ARTICLE

Trace element geochemistry of magnetite from the Cerro Negro Norte iron oxide–apatite deposit, northern Chile

Eduardo Salazar [1,2] · Fernando Barra [1,2] · Martin Reich [1,2] · Adam Simon [3] · Mathieu Leisen [1,2] · Gisella Palma [1,2] ·
Rurik Romero [1,2] · Mario Rojo [4]

Abstract
Kiruna-type iron oxide–apatite (IOA) deposits constitute an important source of iron and phosphorus, and potentially of rare earth elements (REE). However, the origin of IOA deposits is still a matter of debate with models that range from a purely magmatic origin by liquid immiscibility to replacement of host rocks by hydrothermal fluids from different sources. In order to better constrain the origin of Andean IOA deposits, we focused on the Cretaceous Cerro Negro Norte deposit located in the Chilean Iron Belt, northern Chile. The Cerro Negro Norte magnetite ore is hosted in andesitic rocks and is spatially and genetically associated with a diorite intrusion. Our results show that the deposit is characterized by three main mineralization/ alteration episodes: an early Fe–oxide event with magnetite and actinolite followed by four stages that comprise the main hydrothermal event (hydrothermal magnetite + actinolite; calcic–sodic alteration + sulfides; quartz–tourmaline and propylitic alteration) and a minor supergene event. Based on textural and chemical characteristics, four different types of magnetite are recognized at Cerro Negro Norte: type I, represented by high-temperature (∼ 500 °C) magnetite cores with amphibole, pyroxene, and minor Ti–Fe oxide inclusions; type II, an inclusion-free magnetite, usually surrounding type I magnetite cores; type III corresponds to an inclusion-free magnetite with chemical zoning formed under moderate temperatures; and type IV magnetite contains abundant inclusions and is related to low-temperature (∼ 250 °C) hydrothermal veinlets. Electron probe and laser ablation ICP-MS analyses of the four magnetite types show that the incorporation of Al, Mn, Ti, and V into the magnetite structure is controlled by temperature. Vanadium and Ga concentrations are relatively constant within each magnetite type, but are statistically different among magnetite types, suggesting that both elements could be used to discriminate between magmatic and hydrothermal magnetite. However, our results show that the use of elemental discrimination diagrams should be coupled with detailed textural studies in order to identify superimposed metasomatic events and evaluate the impact of inclusions on the interpretation of microanalytical data. The presence of a distinct textural and chemical variation between magnetite types in Cerro Negro Norte is explained by a transition from high- to low-temperature magmatic-hydrothermal conditions. The microanalytical data of magnetite presented here, coupled with new $\delta^{34}S$ data for pyrite (− 0.5 to + 4.3‰) and U–Pb ages of the diorite (129.6 ± 1.0 Ma), are indicative of a genetic connection between the diorite intrusion and the magnetite mineralization, supporting a magmatic-hydrothermal flotation model to explain the origin of Kiruna-type deposits in the Coastal Cordillera of northern Chile.

Keywords Magnetite · Trace element geochemistry · Andean IOCG clan · Iron oxide–apatite deposits · Chile

---

✉ Fernando Barra
   fbarrapantoja@ing.uchile.cl

[1] Department of Geology and Andean Geothermal Center of
    Excellence (CEGA), FCFM, Universidad de Chile, Plaza Ercilla 803,
    Santiago, Chile

[2] Millennium Nucleus for Metal Tracing Along Subduction, FCFM,
    Universidad de Chile, Santiago, Chile

[3] Department of Earth and Environmental Sciences, University of
    Michigan, 1100 North University Ave., Ann Arbor, MI, USA

[4] Compañía Minera del Pacífico (CMP), Pedro Pablo Muñoz 675, La
   Serena, Chile

Springer

Introduction

The Cretaceous metallogenetic belt located in the Coastal Cordillera of northern Chile extends for more than 1000 km in a roughly north–south direction between 22° and 31° S (Fig. 1). This belt comprises intrusive bodies (~ 190–100 Ma) emplaced along the Atacama Fault System (AFS), volcanic and volcanoclastic rocks of Late Jurassic to Late Cretaceous age, and diverse types of mineral deposits, including stratabound Cu(–Ag), porphyry Cu–Mo(–Au), iron oxide–copper–gold (IOCG), and iron oxide–apatite (IOA) deposits (Ruiz et al. 1965; Espinoza 1990; Sillitoe 2003; Barra et al. 2017). Most IOCG and IOA deposits are located in the southern portion of this metallogenetic belt (26° to 30° S), which is known as the Chilean Iron Belt (Fig. 1).

Iron oxide–Cu–Au and IOA deposits constitute end-members of a diverse group of ore deposits which have been classified into the "IOCG clan" (Williams et al. 2005; Barton 2014). IOCG deposits *s.s.* are characterized by a high content of magnetite or hematite with variable concentrations of sulfides (pyrite and chalcopyrite) and where Cu and Au are the economically profitable metals (Williams et al. 2005). Iron oxide–apatite or "Kiruna-type" deposits, on the other hand, are mostly magnetite-rich deposits with abundant actinolite, minor hematite (martite), and apatite, and are mined for their iron ore. In the Chilean Iron Belt, these deposits were mostly

Fig. 1 Map showing the location of the Cerro Negro Norte IOA deposit within the Coastal Cordillera of northern Chile. Other ore deposits from the Cretaceous metallogenetic belt are also shown
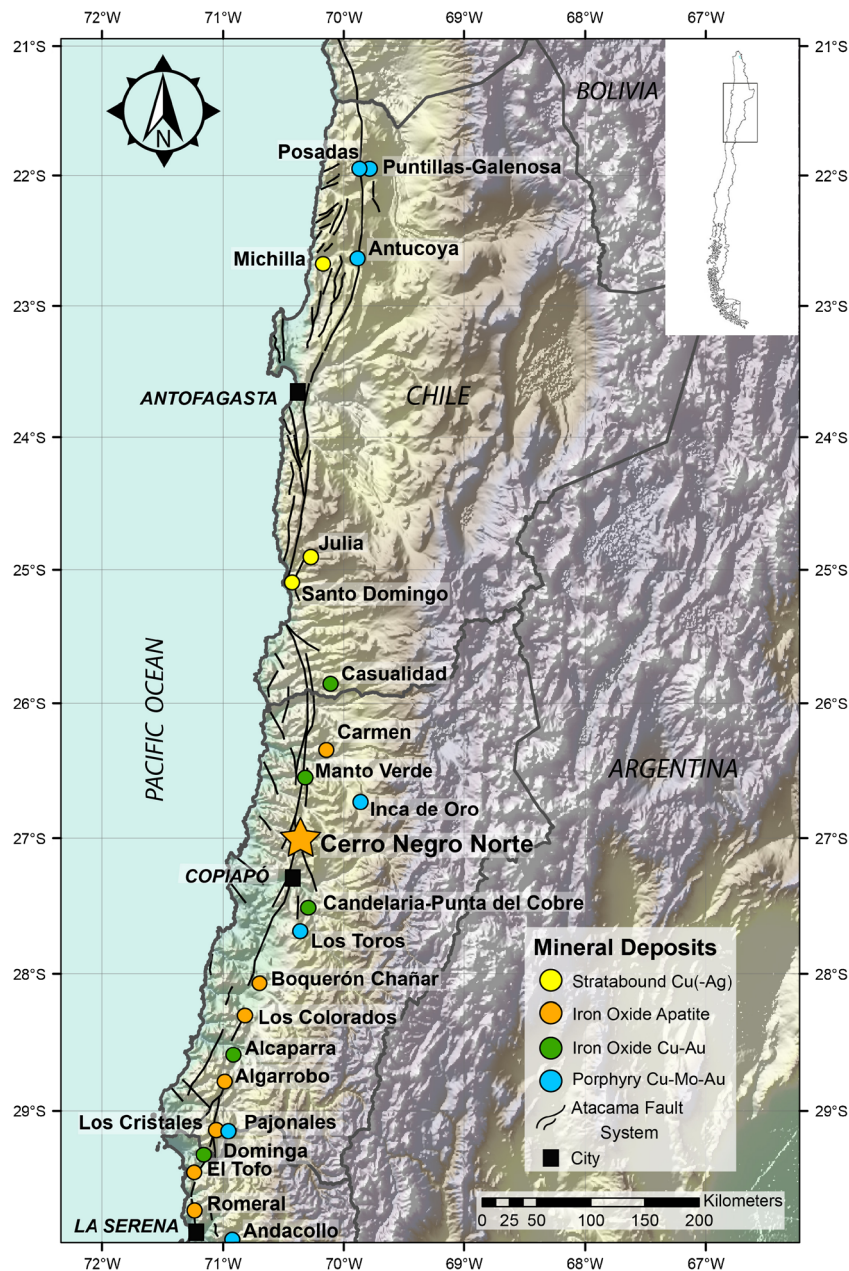
emplaced in volcanic rocks formed within a back-arc basin tectonic setting developed in an active subduction context during the Upper Jurassic–Lower Cretaceous (Aguirre 1985; Mpodozis and Ramos 1990).

The large variability of geological and mineralogical characteristics found in deposits of the IOCG clan has resulted in several disagreements regarding their origin. Recent Re–Os isotope data on IOCGs show that for Andean deposits, the source of metals and fluids is of magmatic-hydrothermal origin, whereas for other IOCGs (e.g., Lala, China, Zhimin and Yali 2013; Olympic Dam, Australia, McInnes et al. 2008) their higher Re and Os concentrations and higher radiogenic Os initial ratios indicate a more crustal source for the metals, where basinal brines could have been involved (Barra et al. 2017). These findings support the idea that IOCG hydrothermal deposits can be formed by different sources and processes. In addition, the origin of IOA deposits is also subject of controversy. Some authors (e.g., Nyström and Henríquez 1994; Tornos et al. 2016) interpret them as formed by an immiscible magnetite-rich melt with a high oxygen fugacity and volatile content, which would reduce its density allowing its ascent to shallow crustal levels. In contrast, other authors indicate that these deposits were formed by hydrothermal replacement of volcanic host rocks (e.g., Sillitoe and Burrows 2002), caused by Fe-rich fluids of magmatic or non-magmatic origin (Ménard 1995).

Several recent studies have focused on the chemistry of magnetite (Fe_3O_4) to provide some insights on the formation of the different magnetite-bearing deposits (Dare et al. 2014; Nadoll et al. 2014). Magnetite is a ubiquitous mineral phase in different geological environments and the specific conditions at which magnetite crystallized are reflected in its trace element composition (e.g., Loberg and Horndahl 1983; Dare et al. 2014, 2015; Nadoll et al. 2014, 2015; Knipping et al. 2015a, 2015b; Rojas et al. 2018a). Several trace elements can be incorporated into the magnetite structure, e.g., Al, Mn, Ti, V, Ni, Cr, Zn, Co, Sn, Ga, and Mg. Hence, the presence and concentration of these elements have been used to construct discrimination diagrams (Dupuis and Beaudoin 2011; Nadoll et al. 2014; Dare et al. 2014; Wen et al. 2017) and to explain the chemical variation of magnetite for any particular deposit. In addition, improvements in analytical techniques, such as laser ablation inductively coupled plasma mass spectrometry (LA-ICP-MS), have made it possible to precisely measure these trace elements, resulting in a better discrimination between hydrothermal and magmatic magnetite (Nadoll and Koenig 2011; Dare et al. 2014; Nadoll et al. 2014).

Recently, Knipping et al. (2015a, 2015b) used the trace element composition of different textural types of magnetite identified at the Los Colorados IOA deposit to propose a novel "flotation model" to explain the formation of IOA deposits. This model involves the crystallization of igneous magnetite microlites within a cooling silicate magma that ascends by interaction with fluids exsolved from the silicate melt. The

ascending magnetite-fluid suspension coalesces to form the massive magnetite ore bodies in regional-scale transcurrent faults. In addition, the high-salinity hydrothermal fluids that nucleate on magnetite grains will not only extract Fe from the magma but also other metals such as Cu and Au, which would lead to the precipitation of copper sulfides and hydrothermal magnetite at cooler and shallower levels forming in some cases an IOCG-type deposit (Knipping et al. 2015a, 2015b; Reich et al. 2016; Barra et al. 2017; Rojas et al. 2018a, 2018b). The flotation model is supported by variations in the mineral chemistry observed in different textural types of magnetite at the Los Colorados (Knipping et al. 2015a, 2015b) and El Romeral (Rojas et al. 2018a) IOA deposits in the Chilean Iron Belt. The chemical composition of the magnetite grains reflects their formation conditions, from purely magmatic at deeper levels of the mineral system to low-temperature hydrothermal at shallow levels. Further evidence for a magmatic component is supported by stable Fe and O isotope data determined in magnetite from Los Colorados (Bilenker et al. 2016; Knipping et al. 2019). Thus, the flotation model not only reconciles the magmatic with the hydrothermal model but also provides a consistent explanation for the genetic relation between IOA and IOCG deposits in the Andean IOCG province (Simon et al. 2018).

The Cretaceous Chilean Iron Belt is an ideal site to study the formation of IOA deposits because their primary geologic features remain mostly undisturbed by later superimposed metamorphic or metasomatic events. The present work focuses on the Cerro Negro Norte IOA deposit located in the Coastal Cordillera of northern Chile, near the city of Copiapó (Fig. 1). The main purpose of this study is to provide new constraints on the formation of Andean IOA deposits using field observations, petrographic and textural studies, geochronology, mineral chemistry (EPMA and LA-ICP-MS), and sulfur isotope data for the Cerro Negro Norte deposit.

Geological background

The Coastal Cordillera of northern Chile comprises several dioritic to monzodioritic plutonic complexes with ages ranging from ca. 190 to 100 Ma (Grocott and Taylor 2002). These complexes intrude thick piles of volcanic and volcanoclastic rocks formed in an intra or back-arc environment, mainly represented by the Jurassic La Negra and the Early Cretaceous Punta del Cobre and Bandurrias formations (Lara and Godoy 1998; Arévalo 2005). The extensive Middle Jurassic to Early Cretaceous igneous activity that characterizes the Coastal Cordillera occurred under extensional conditions in response to the slab roll-back and the Mariana-type high-angle subduction (Mpodozis and Ramos 1990; Grocott and Taylor 2002). Along the Coastal Cordillera of northern Chile and southern Peru, the western portion of the Mesozoic arc and its respective fore-arc appear to have been

removed by subduction erosion or lateral displacement (Mpodozis and Ramos 1990).

The Cretaceous Chilean Iron Belt (CIB), located in the Coastal Cordillera between 26° and 30° S, corresponds to a longitudinal belt of iron-rich deposits that extends for over 600 km. The CIB is coincidental with the position of an Albian intrusive belt (~ 130–100 Ma) and the southern portion of the Atacama Fault System. The IOA deposits (e.g., Los Colorados, El Algarrobo, El Romeral, Cerro Negro Norte) are mostly hosted in volcanic rocks assigned to the La Negra, Bandurrias, or Punta del Cobre formations (Segerstrom 1968; Vivallo et al. 1995a, 1995b), which accumulated in an arc/back-arc basin system developed during the Late Jurassic to Early Cretaceous.
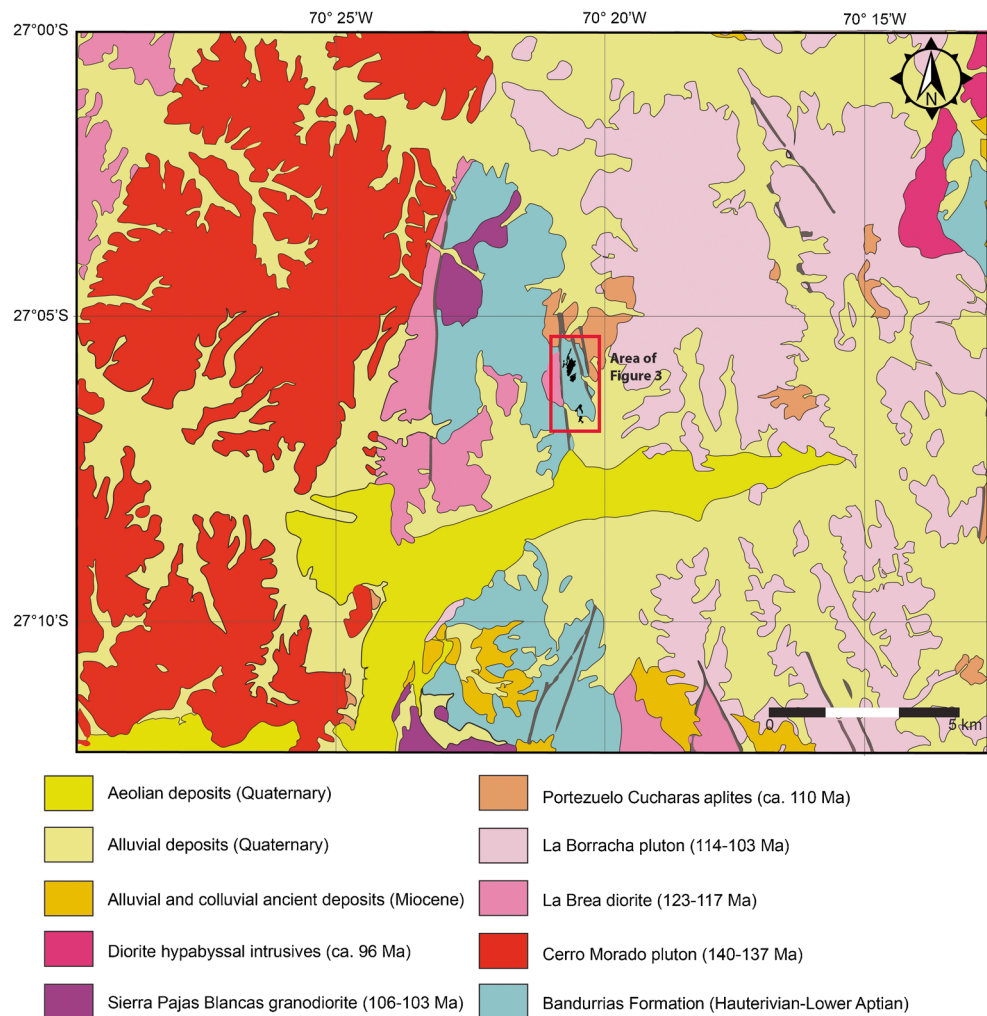
Geology of the Cerro Negro Norte deposit

The Cerro Negro Norte IOA deposit is located at 27° 05′ S and 70° 21′ W (Fig. 1), approximately 37 km northwest of Copiapó, and is hosted in volcanic and volcanoclastic rocks of the Bandurrias Formation (Fig. 2). The deposit is currently mined by Compañía Minera del Pacífico (CMP), and estimated resources are at 657.3 Mt with an average grade of 29.7% Fe (CAP Minería Annual Report 2016). The Cerro Negro Norte host rocks are breccias and andesitic lavas that represent a roof pendant of volcanic rocks interspersed with granitoids. To the east, the Cerro Negro Norte deposit is limited by the Portezuelo Cucharas aplites and the La Borracha pluton (Fig. 2). To the west, the deposit is limited by the La Brea diorite (123–117 Ma, Arévalo 1995) and the Sierras Pajas Blancas granodiorite (K–Ar age of 103 ± 5 Ma; Arévalo 1995; Fig. 2).

Small monzodiorite to granodiorite intrusions and dikes are present in the district. These dikes have a general NNE orientation and intrude the diorite and quartz–diorite stocks, as well as the andesite and magnetite bodies (Vivallo et al. 1995a; Raab 2001) (Fig. 3). Post-mineral andesite dikes striking NNE and EW have been reported in the Abanderada, Veta Central, and NE of the Beduino area (Raab 2001; Fig. 3). West of the Abanderada area, these dikes appear to be related to sulfide (pyrite + chalcopyrite) mineralization (Raab 2001). In general, these rocks have up to 2% of disseminated

Fig. 2 Geology of the Cerro Negro Norte district. Modified from Arévalo (2005)

Legend:
- Aeolian deposits (Quaternary)
- Alluvial deposits (Quaternary)
- Alluvial and colluvial ancient deposits (Miocene)
- Diorite hypabyssal intrusives (ca. 96 Ma)
- Sierra Pajas Blancas granodiorite (106-103 Ma)
- Portezuelo Cucharas aplites (ca. 110 Ma)
- La Borracha pluton (114-103 Ma)
- La Brea diorite (123-117 Ma)
- Cerro Morado pluton (140-137 Ma)
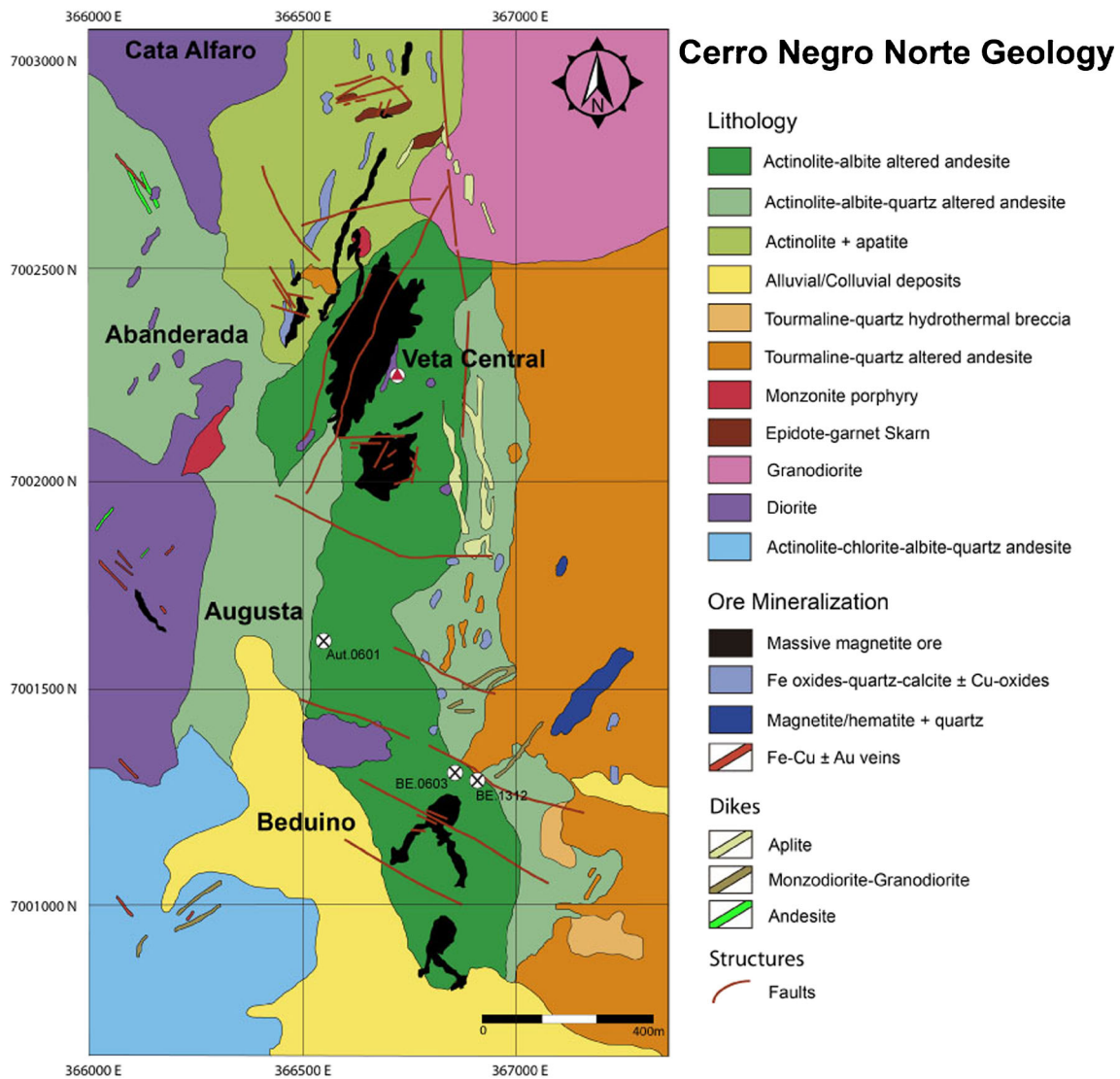- Bandurrias Formation (Hauterivian-Lower Aptian)

Fig. 3 Geologic map of Cerro Negro Norte deposit. Modified from CMP unpublished map

magnetite and are altered to actinolite, chlorite, epidote, calcite with minor sericite, and unspecified clays.

Minor mylonite zones up to 50 m thick have been described at the contact between the andesite and the diorite (Vivallo et al. 1995a; Raab 2001). These mylonites are dominated by actinolite, which occurs both in the groundmass and in bands up to 4 mm thick. Locally, veinlets of scapolite + actinolite + titanite are observed cross-cutting magnetite veins. These, in turn, cut banded mylonite with scapolite and moderately altered pyroxene (Raab 2001).

The Cerro Negro Norte deposit comprises five magnetite ore zones from north to south: Cata Alfaro, Abanderada, Veta Central, Augusta, and Beduino (Fig. 3). Massive magnetite forms vertical to subvertical elongated bodies, tabular to lobular in shape, with a general NS orientation and distributed in an area of about 0.5×5.0 km^2. The mineralization includes large amounts of magnetite locally altered to hematite (martitization), minor sulfides (pyrite +chalcopyrite), and local copper oxides. The iron ore bodies consist of massive and disseminated magnetite with actinolite and minor apatite, pyrite, and chalcopyrite. According to their textural characteristics, the magnetite ore can be classified as massive, brecciated, stockwork, and disseminated. These bodies may exhibit abrupt contacts (e.g., eastern Abanderada) or gradational with respect to the host rock (e.g., western Abanderada, Veta Central). In addition, north of the Abanderada area, there are tabular magnetite bodies with NNE orientations that would indicate areas of weakness and fluid circulation (Raab 2001). Subhorizontal massive ore bodies a couple of meters thick, with variable extension and shape, show sharp contacts with the andesite rock in the Veta Central and Cata Alfaro areas (Vivallo et al. 1995a; Raab 2001). These bodies are usually interstratified with volcanic rocks, a feature that has been interpreted as a complete replacement of andesitic lava flows by the magnetite (Raab 2001) or as intrusive or extrusive bodies of magnetite (Vivallo et al. 1995a). Disseminated

magnetite mineralization occurs mainly in the andesitic host rocks and, to a lesser extent, in diorite or monzodiorite–granodiorite dikes. Brecciated magnetite bodies are described to the east of Abanderada, north of Veta Central, and Cata Alfaro. In addition, magnetite clasts were observed in quartz–diorite igneous breccias that are spatially associated with monzodiorite and granodiorite dikes (Raab 2001).

Hydrothermal alteration is defined by a pervasive actinolitization of the andesitic host rocks around the magnetite ore (Fig. 3), grading outward to an actinolite–albite ± quartz zone. To the east, a tourmaline–quartz zone is dominant and in which andesite clasts are pervasively albitized with local presence of K-feldspar (Vivallo et al. 1995a; Raab 2001).

Analytical methods

Samples were collected from the Beduino (drill cores BE.1312: 248 m and BE.0603: 342 m) and Augusta (drill core Aut.0601: 215 m) ore bodies (Fig. 3). Additional samples were collected in the Veta Central pit. Drill hole Aut.0601 cuts the main ore body at depth, whereas the Beduino drill holes cut minor ore bodies located at the southern part of the deposit (Fig. 3). Thin and thick sections (100 μm) were made for petrography and for electron probe microanalysis (EPMA), and laser ablation inductively coupled plasma mass spectrometry (LA-ICP-MS) measurements, respectively. Samples were studied under a polarized light microscope and by using a FEI Quanta 250 scanning electron microscope (SEM) equipped with secondary electron (SE), backscattered electron (BSE), and cathodoluminescence (CL) detectors, and a solid-state X-ray energy-dispersive spectrometer (EDS) at the Andean Geothermal Centre of Excellence (CEGA), Universidad de Chile, to identify and characterize the ore and alteration mineralogy. Microanalytical methods used in this study are detailed below.

Microanalysis and elemental mapping The electron probe microanalyses were performed at the Michael J. Drake Electron Microprobe Laboratory, University of Arizona, Tucson, USA. Concentrations of Al, Si, Cr, Ti, V, Ca, Fe, Mn, Mg, Zn, Ni, Cu, Na, and K were determined in magnetite by using a Cameca SX-100 instrument (Table SM1). A focused beam (2 μm) was used to avoid hitting any inclusions or exsolution lamellae within the grains. Analytical conditions were 40° take-off angle, a beam energy of 15 keV, and a current of 20 nA. In addition, wavelength-dispersive spectrometry (WDS) X-ray maps were acquired by using an accelerating voltage of 15 kV, a beam current of 80 nA, and a counting time of 12 ms/step.

Trace element analysis Laser ablation-ICP-MS measurements were performed on magnetite grains from six samples collected at different depths by using a Photon Machines Analyte G2 193-nm ArF excimer laser ablation coupled to a Thermo Fisher

Scientific iCAP-Q quadrupole mass spectrometer at the CEGA Mass Spectrometry Laboratory, Department of Geology, Universidad de Chile. The mass spectrometer was tuned to high sensitivity and a simultaneous low oxide formation rate (ThO/Th < 0.5). Since helium was used as a carrier and argon as a plasma gas, interferences with these elements as well as with oxides of these elements and double charged ions were taken into account when choosing representative isotopes for each element. Thus, ^{57}Fe was measured for the iron content, instead of the more abundant ^{56}Fe that has interference with ArO. Thirty seconds of background were measured for baseline correction prior to sample analysis, and a sample-standard bracketing method (2 × standard, 2 × secondary standard, 18 × samples, and 2 × standard) was used for instrumental drift correction.

The USGS GSE-1G reference material was used for magnetite analysis and the USGS GSD-1G as a secondary standard. The iron concentration of magnetite determined by EPMA was used as the internal standard. The Al and V content determined by LA-ICP-MS is in good agreement with concentrations determined by EPMA, which supports the use of the GSE-1G reference material as a suitable standard for magnetite laser ablation analysis. A 40-μm laser spot size was used for measurements, which was the best compromise between analyzing inclusion-free areas and measuring above the detection limit of most elements. In total, 37 elements were measured with dwell times of 10 ms to achieve measurable concentrations of these elements. Analyses were performed by using a laser repetition pulse of 5 Hz for 60 s per each spot with a fluence of 4.0 J/cm^2. Data reduction was carried out with the Iolite software (Paton et al. 2011), which calculates detection limits after Longerich et al. (1996). The influence of micro- to nanometer-sized inclusions within magnetite growth zones (Deditius et al. 2018) could not be totally avoided due to the laser beam size. Analyses affected by the presence of such inclusions—as determined by irregular, spiky element signals—were removed from the dataset. The concentration and concentration uncertainty for each element were calculated using Iolite and are reported in Table SM2.

U–Pb dating Uranium–lead dating was carried out on zircon grains extracted from a diorite sample from the Veta Central pit (Fig. 3), which possibly corresponds to La Brea diorite. Zircon grains were separated at the Zirchron LLCC (Tucson, Arizona) using electro-pulse disaggregation. The disaggregated sample was sieved and collected into a water beaker. The fine, light fraction was removed from the water and the mineral concentrate was then sieved through a 50′ mesh (300 μm). The dried sample was later passed through an LB-1 Frantz Magnetic Barrier Separator to remove the magnetic fraction. Finally, a heavy liquid (methylene iodide) was used to collect the zircons by decantation.

Mounting and isotopic analyses were carried out at the CEGA Mass Spectrometry Laboratory, Universidad de

Chile. Zircons were mounted in epoxy resin and later polished. Cathodoluminescence images were obtained by using a Centaurus CL detector coupled to an SEM. For U–Pb dating, a laser ablation system (Analyte G2) coupled to an iCAP-Q mass spectrometer was employed. A spot size of 50 μm, a repetition rate of 10 Hz, and a fluence of 2.5 mJ/cm^2 were used for the U–Pb analyses. A sample bracketing method was performed with Plešovice (Sláma et al. 2008) and Temora2 (Black et al. 2004) reference materials. Data reduction was performed by using Iolite (Paton et al. 2011) and the statistical process was done with Isoplot 4.0 (Ludwig 2010).

Sulfur isotopes Stable isotopes of sulfur were measured in pyrite from seven samples; two corresponding to drill core BE.1312, three from drill core BE.0603, and two from drill core Aut.0601. Pyrite concentrates were prepared by grinding the samples using a stainless steel mortar, followed by handpicking of pyrite grains by using titanium tweezers to avoid grains with visible impurities. The mineral concentrates were sent to the Environmental Isotope Laboratory, Department of Geosciences, University of Arizona, Tucson, AZ. A continuous-flow gas-ratio mass spectrometer (CF-IRMS) ThermoQuest Finnigan Delta PlusXL model with a Costech elemental analyzer was used for $^{34}S/^{32}S$ ratio measurements. The sulfide grains were introduced into a combustion chamber with O_2 and V_2O_5 (Coleman and Moore 1978) obtaining an SO_2 gas at 1030 °C, which is the analyzed product. The system was calibrated by using the international standards OGS-1, which is a $BaSO_4$ precipitated from seawater, and NBS123, a sphalerite sample with a $\delta^{34}S$ value of + 17.09‰. A linear calibration between − 10 and + 30‰ was used and a precision of ± 0.15 or 1σ was estimated by diverse internal standards measurements. Sulfur isotope data are reported in delta notation as per mil (‰) values, where $\delta^{34}S = [[(^{34}S/^{32}S)_{sample} − (^{34}S/^{32}S)_{standard}]/(^{34}S/^{32}S)_{standard}] \times 1000$.

Results

Rock types

The andesitic rocks are characterized by their gray to dark-green color and a porphyritic texture with up to 25% modal of subhedral to euhedral plagioclase phenocrysts ranging in size from 0.5 to 3 mm long (Fig. SM1a). Phenocrysts of clinopyroxene (up to 0.5 mm) and hornblende (up to 2.5 mm) are also observed and may reach up to 10% modal of the sample. The fine-grained groundmass is dominated by plagioclase with minor quartz and clinopyroxene. Variable amounts of hydrothermal mineral phases, such as scapolite, albite, epidote, titanite, quartz, calcite, chlorite, and sericite,

are also observed in the altered andesite rocks. At the eastern margin of the deposit, the andesite is almost completely altered to tourmaline with quartz, minor sericite, and chlorite. The contact between the andesite and the intrusive rocks at the eastern flank is not well defined due to pervasive hydrothermal alteration. The magnetite ore is hosted mostly in the andesite.

Diorite intrusions (Fig. SM1b) are present at the western part of the deposit (Fig. 3). These rocks have an equigranular texture with 50–75% modal of subhedral to euhedral plagioclase with concentric oscillatory zoning. Quartz is usually less than 10% modal but can reach up to 20% modal. The rocks show a calcic and sodic alteration with actinolite and subordinate epidote replacing primary pyroxene and amphibole, and scapolite + albite ± sericite replacing plagioclase. Titanite is a common and ubiquitous alteration phase in these rocks, especially south of the Abanderada area, where it can reach up to 10% modal (Raab 2001). The quartz–diorite rocks show up to 70% modal of partially sericitized plagioclase, chlorite after actinolite, and up to 15% modal anhedral quartz.

Hydrothermal alteration

Four main alteration types are observed in Cerro Negro Norte.

Actinolitization It corresponds to the main alteration style and represents the earliest alteration event in the deposit. It preferably affects the andesite host rocks; however, it is also observed as an alteration phase in the diorite intrusions. Actinolite is usually dark-green and fine- to coarse-grained and occurs as large aggregates spatially associated with massive magnetite (Fig. SM1c), veinlets ranging from 1 mm to 10 cm in thickness (Fig. SM1d), and replacing hornblende and pyroxene.

The actinolitized rocks are partially altered to chlorite and sometimes include calcite and quartz. Actinolite veinlets can be associated with scapolite ± apatite ± plagioclase ± quartz ± sulfides (Fig. SM1d). Large actinolite crystals, with or without preferred orientation, are observable in thin section (Fig. 4a), where it is also evident that the actinolite-rich calcium alteration precedes the sodium alteration with scapolite and albite.

Calcic–sodic alteration This alteration type is characterized by a scapolite-rich and an albite-rich alteration zone, both with variable amounts of actinolite. Scapolite alteration is more abundant near the magnetite ore bodies where it is observed as large granular aggregates and thick veinlets mostly associated with the quartz–diorite stocks located SW of Beduino (Fig. 3). At a more distal position from the ore bodies, albite predominates over scapolite, which is present as fine disseminations and in veinlets with epidote and quartz.

Fig. 4 Cross polarized photomicrographs of different alteration types at Cerro Negro Norte. a Elongated prismatic actinolite (act) crystals with quartz (qtz) and chlorite (chl). b Tabular aggregates of euhedral apatite (ap) and subhedral scapolite (scp) with magnetite (mt) and actinolite (act). c Tabular aggregates of scapolite (scp) with fine-grained biotite (bt) and magnetite (mt). d Fibrous actinolite (act) crystals intergrowth with plagioclase (pg) and sericite (ser). e Tourmaline (tur) crystals with albite (ab), quartz, and disseminated magnetite (mt). f Actinolite (act) replaced by an assemblage of chlorite (chl), calcite (cal), and quartz (qtz)
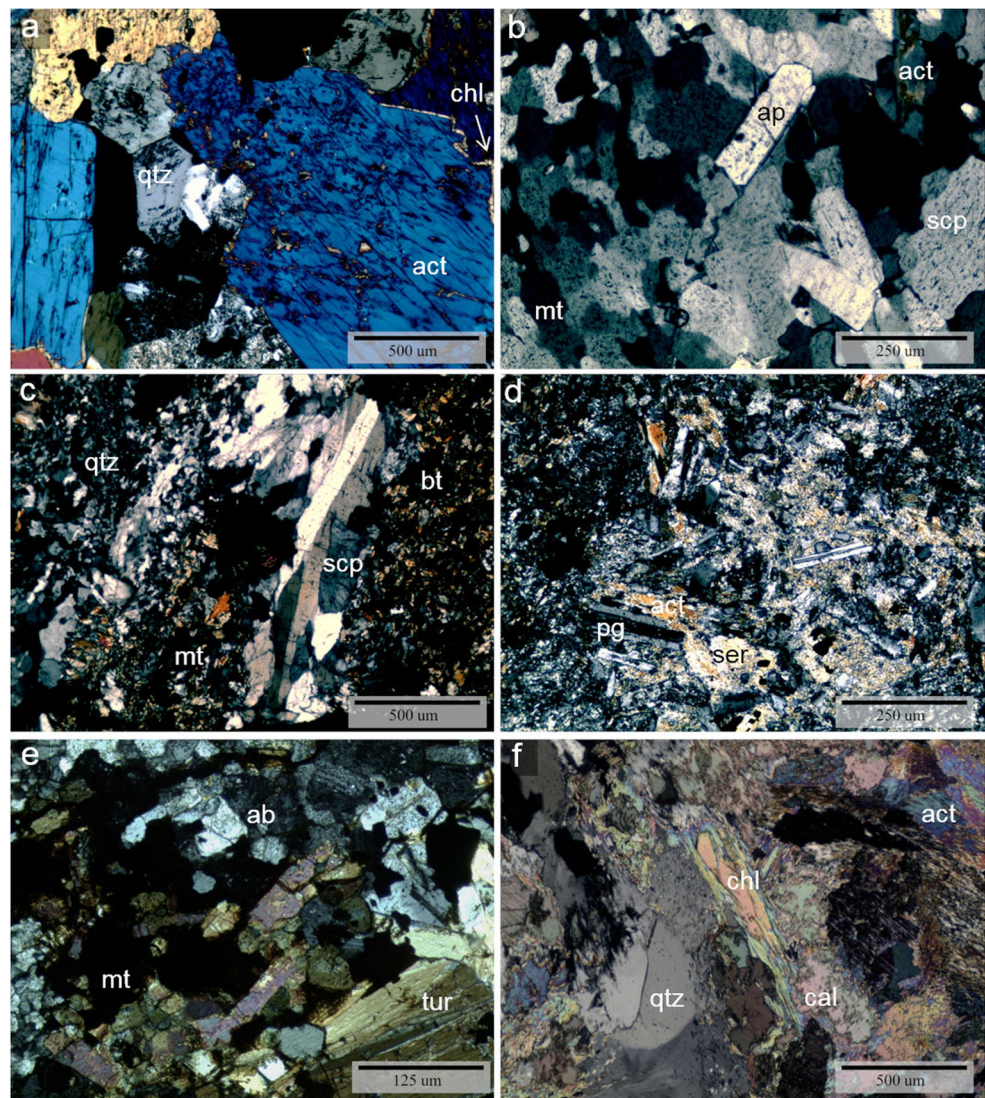
In thin section, scapolite appears as anhedral to subhedral granular aggregates intergrown with actinolite, magnetite, and minor apatite (Fig. 4b) or associated with titanite + epidote ± biotite ± magnetite ± calcite ± apatite (Fig. 4c) and with relict clinopyroxene in areas poorly affected by actinolitization. Locally, it is observed as a replacement of euhedral plagioclase in andesite.

Albite occurs as a pseudomorphic replacement of primary plagioclase in andesite and less frequently in veinlets with actinolite + epidote + magnetite ± calcite ± titanite. In some cases, plagioclase is altered to sericite (Fig. 4d) or to an assemblage of chlorite, epidote, and iron oxides.

Quartz-tourmaline alteration Tourmaline + quartz + sericite hydrothermal breccias (Fig. SM1e) and andesites and diorites pervasively altered to tourmaline + quartz + sericite + chlorite are observed at the eastern part of the deposit (Fig. 3).

Tourmaline breccias have been interpreted as formed after the calco-sodic alteration (Vivallo et al. 1995a).

Petrographic studies show several crystal habits for tourmaline (Fig. 4e), which include sub-triangular euhedral grains with zonations, fine euhedral disseminations, anhedral to subhedral radial needles, and veinlets. When it appears as interpenetrating tabular or acicular aggregates, the crystals can measure up to 2 mm in length.

Propylitic alteration It corresponds to the chlorite + quartz + calcite ± epidote ± sericite association (Fig. 4f). Chlorite is commonly found as a replacement of actinolite in andesite, intrusive rocks, and ore bodies, as well as in sheeted aggregates and interstitial granular aggregates in the groundmass. Veinlets of chlorite + calcite with minor copper carbonates are also observed. In addition, primary plagioclase can be replaced by calcite and locally by titanite. Minor epidote and quartz form anhedral granular aggregates and fine veinlets.

Raab (2001) interpreted this propylitic alteration as a distal and gradational assembly from albite-rich associations, overlapping with calco-sodic alteration.

Mineralization

The massive iron ore body comprises anhedral to euhedral granular aggregates of magnetite with medium to low integrity and abundant silicate inclusions (Fig. 5a). The magnetite granular aggregates are usually intergrown with actinolite and can be in contact with pyrite or chalcopyrite (Figs. SM1f, 5b-f), apatite, and titanite. Hematite is observed as small patches within magnetite (Fig. 5a) and as a thin rim on magnetite or pyrite (Fig. 5b).

Sulfide mineralization is moderate to minor and comprises mainly pyrite and chalcopyrite and lesser amounts of bornite, pyrrhotite, covellite, and digenite. Pyrite and chalcopyrite are found as inclusions within magnetite grains (Figs. SM1f, 5a) but more commonly as veinlets, and as subhedral to anhedral disseminated grains in the silicate matrix or in simple contact with magnetite (Fig. 5b, c). Chalcopyrite also occurs as inclusions in pyrite (Fig. 5b–e) and in the interstices between magnetite grains (Fig. 5d, f). Pyrrhotite is present as small, droplet-shaped inclusions in pyrite, whereas digenite and covellite are found as replacements of bornite and chalcopyrite (Fig. 5e, f).

Sulfide veinlets of pyrite ± chalcopyrite are mostly related to the Ca–Na alteration stage, whereas scarce calcite + Cu–carbonate veinlets are associated with the propylitic alteration. Near or at the surface, sulfides are almost completely oxidized forming jarosite, goethite, and minor Cu oxides.

In summary, three main mineralization/alteration events are recognized in the Cerro Negro Norte deposit (Fig. 6). The first stage corresponds to the main iron oxide mineralization event represented by massive magnetite mineralization with actinolite and minor apatite, and scarce sulfide inclusions (Fig. 5a).

Fig. 5 Reflected light photomicrographs of ore mineralization at Cerro Negro Norte deposit. a Granular aggregate of magnetite with pyrite (py), chalcopyrite (ccp) inclusions, and hematite (hm) patches. b Simple contact between magnetite (mt) and pyrite (py) grains with hematite (hm) along the grain boundaries. Also, chalcopyrite (ccp) is present as inclusion in pyrite. c Anhedral pyrite grain with chalcopyrite (ccp) and pyrrhotite (po) inclusions. d Chalcopyrite (ccp) filling spaces between magnetite grains. e Bornite (bo), chalcopyrite (ccp), and pyrite (py) immersed in an actinolite matrix. Bornite is slightly replaced by digenite (dg), and pyrite (py) shows chalcopyrite (ccp) and pyrrhotite (po) inclusions. f Chalcopyrite (ccp) in contact with actinolite (act) and magnetite (mt). Digenite (dg) is observed as an incipient replacement of chalcopyrite
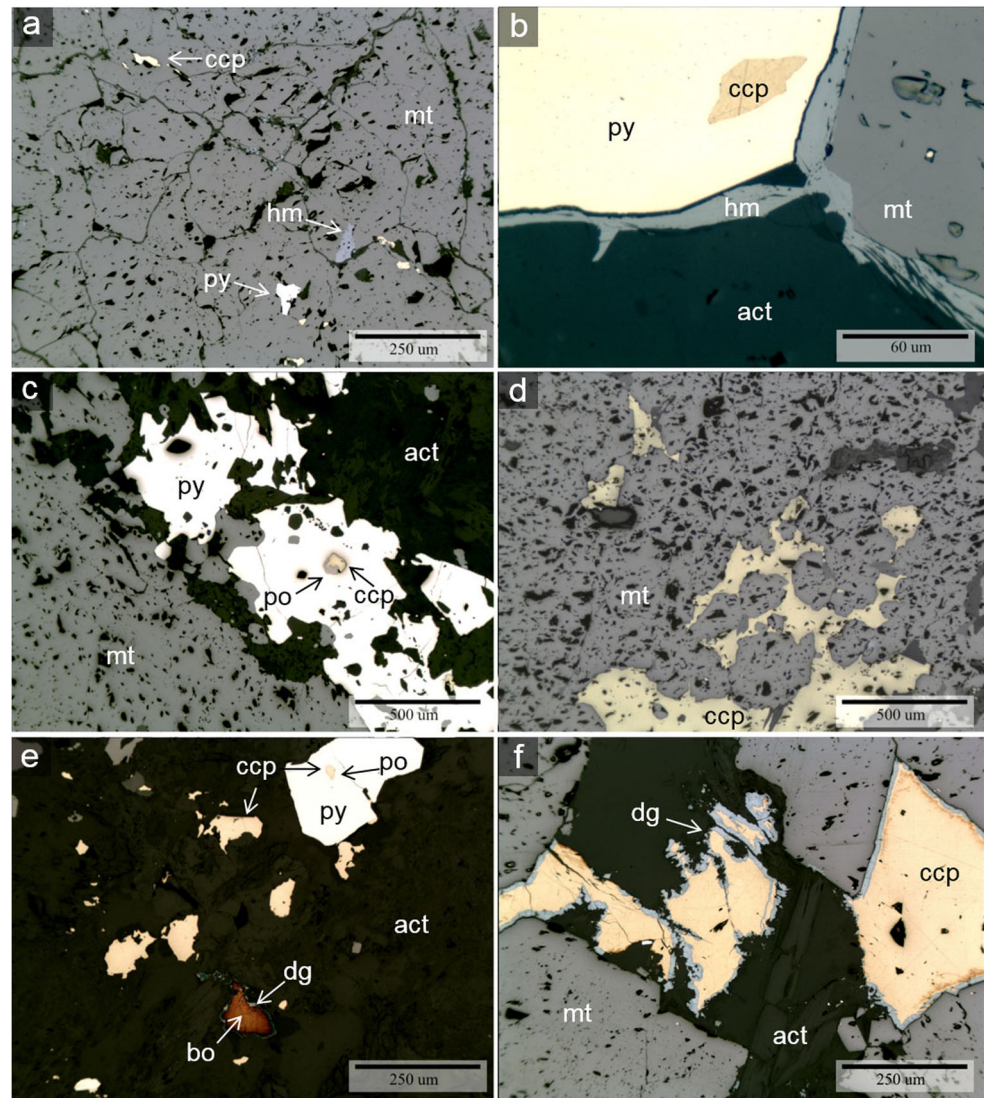
This event is followed by the main hydrothermal event, which is divided into four stages. Stage I is characterized by hydrothermal magnetite and abundant actinolite (Fig. 4a); stage II is represented by pyrite + chalcopyrite ± pyrrhotite ± bornite and corresponds to the main sulfide event associated with the Ca–Na alteration. The sulfide mineralization is present as disseminations within the silicate matrix (Fig. 5e), between magnetite grains (Fig. 5c, d), and mainly as veinlets dominantly controlled by shear zones or NNW faults (Vivallo et al. 1995a, 1995b; Raab 2001). Stage III is the quartz–tourmaline breccia event described above (Fig. SM1e), and stage IV corresponds to the propylitic alteration (chlorite–calcite) with sulfide veinlets and minor Cu carbonates. The last event is the supergene stage, characterized by iron oxides and hydroxides, minor copper oxides, and replacement of primary sulfides by digenite or covellite (Fig. 5e, f). Although no gold grains were observed in our samples, previous studies indicate that gold is spatially associated with the pyrite ± chalcopyrite veins and the quartz–tourmaline alteration (Vivallo et al. 1995b; Raab 2001).

Magnetite textures and chemistry

Different magnetite types were identified based on textures (Fig. SM2). The most relevant types are magnetite type I, which contains abundant inclusions, and inclusion-free magnetite type II (Fig. SM2a,b). In magnetite type I, inclusions vary in size from nanometer size to a few tens of micrometers that are randomly distributed or are arranged following crystallographic planes in magnetite. In general, the inclusion-free magnetite (type II) is observed as an overgrowth on inclusion-rich type I magnetite grains. These two magnetite types account for more than 90% modal of magnetite in the ore bodies. A third type of magnetite (type III) is observed as large (up to 100 μm across) sub- to idiomorphic octahedral grains with an inclusion-free core and a cryptic zonation towards the rim of the crystal (Fig. SM2c). Type IV magnetite corresponds to a late magnetite vein event that cross-cuts all other magnetite types. Some of these magnetite grains display micron- to submicron-sized inclusions arranged in sinuous oscillatory zoning (Fig. SM2d).

The concentrations of Fe, Si, Al, Ca, Na, K, and V were measured by using EPMA. However, most of the measurements were below the detection limit except for Fe, V, Si, and Al (Table SM1). X-ray elemental maps for individual grains were also obtained by using WDS (Fig. SM3). A general trend of depletion in Mg, Al, Ca, Mn, and Ti was identified from core (type I) to rim (type II) (Fig. SM2a,b). Nevertheless, some magnetite rims show a slight enrichment in Ti and Al (type II; Fig. SM3a); Ti, Mg, and Si (type III, Fig. SM3b); and Mg, Al, and Si (type IV, Fig. SM3c).

As mentioned above, the Fe concentration of magnetite determined by EPMA was used as the internal standard for trace element analysis using LA-ICP-MS. Laser ablation ICP-MS data are summarized in Fig. 7, whereas the maximum,
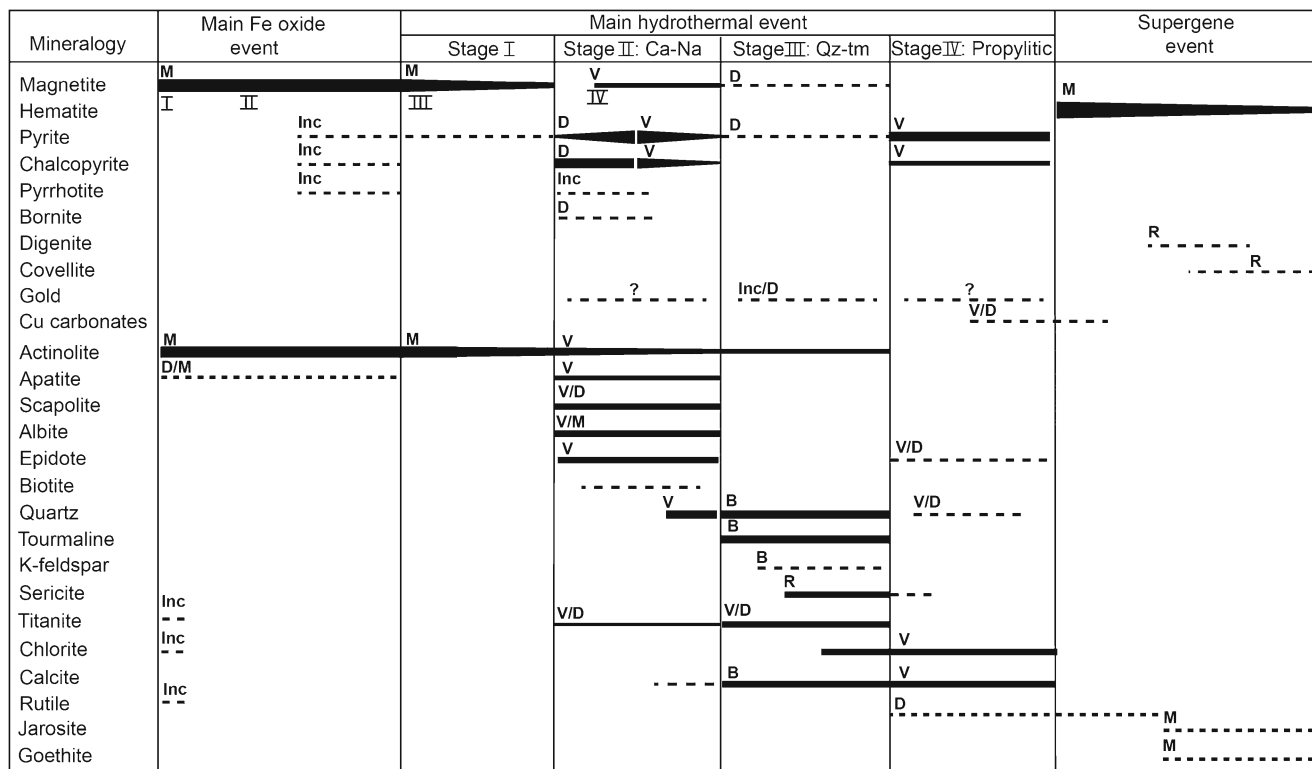

Fig. 6 Paragenetic chart for the Cerro Negro Norte deposit. I, II, III, and IV: magnetite types, M: massive, D: disseminated, V: veinlets, B: breccias, Inc: inclusion

minimum, and average concentration for each element in the four types of magnetite identified in Cerro Negro Norte are reported in Table 1. All results are reported in Table SM2. Based on the average values for each analyzed element (Table 1), the following trends can be recognized: Na, Mg, K, Ca, Mn, Zn, and Ga are most abundant in type I. The average concentration of Ti is similar in types I, II, and III, but the highest values are found in type I (~ 1990 ppm). Vanadium is higher in types I and II, Cu in type III, and P in type IV. Types I and II have similar concentrations of Ni and Co, but the highest average concentrations are found in type IV. Types I and IV display the highest Ba and Sr average concentrations. Germanium is relatively constant in all magnetite types reaching an average of ~ 6 ppm, whereas Y, Nb,

Mo, Sb, and Sn are low with average concentrations below 2 ppm. Chromium and Sc are mostly below their detection limits of 2.4 and 0.8 ppm, respectively (Table 1).

Silicate and oxide inclusions in magnetite

Several types of mineral inclusions were identified by using micro-Raman spectroscopy analysis, SEM, and LA-ICP-MS data. The inclusions can be oriented or randomly distributed, single or polycrystalline. Actinolite is the most ubiquitous phase and can be accompanied by quartz and an unspecified Mg–Al–Si phase. The latter was also reported in magnetite ores from Los Colorados (Knipping et al. 2015b) and El Romeral (Rojas et al. 2018a). Inclusions in type I magnetite
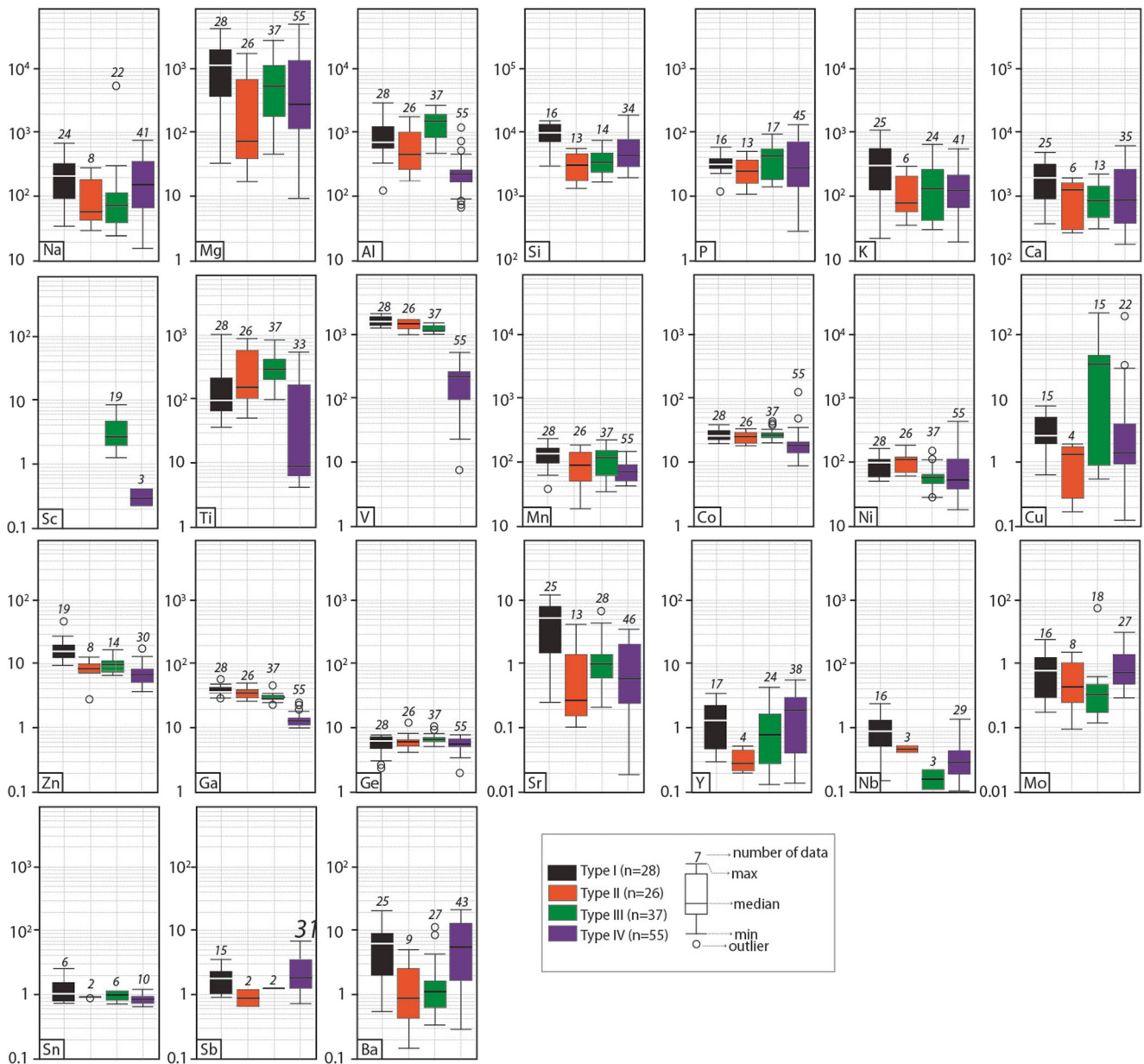

Fig. 7 Statistical summary of trace element concentrations determined by using LA-ICP-MS for the magnetite types described in Cerro Negro Norte

Table 1 Summary of LA-ICP-MS analyses for magnetite types

	DL	N	n	Type I	N	n	Type II	N	n	Type III	N	n	Type IV
Na	13.0	24	4	<13.0–700 *241*	8	18	<13.0–306 *115*	21	16	<13.0–295 *84.9*	41	14	<13.0–710 *210*
Mg	0.17	28	0	32.6–4050 *1405*	26	0	17.2–1850 *419*	37	0	44.1–2690 *724*	55	0	8.54–4360 *913*
Al	0.90	28	0	130–3010 *924*	26	0	180–1910 *669*	37	0	481–2650 *1406*	55	0	67.3–1290 *280*
Si	876	16	12	<876–14,320 *9522*	13	13	<876–5900 *3495*	14	23	<876–7170 *3605*	34	21	<876–18,200 *5558*
P	4.40	16	12	<4.40–58.0 *33.2*	13	13	<4.40–48.0 *25.5*	17	20	<4.40–86.0 *34.7*	45	10	<4.40–143 *48.3*
K	10.5	25	3	<10.5–1105 *372*	6	20	<10.5–320 *134*	24	13	<10.5–613 *187*	41	14	<10.5–635 *184*
Ca	152	25	3	<152–4620 *1963*	6	20	<152–1990 *1150*	13	24	<152–2290 *1056*	35	20	<152–6910 *1640*
Ti	4.00	28	0	70–1990 *330*	26	0	54.7–936 *327*	37	0	101–870 *340*	33	22	<4.0–509 *72.8*
V	0.80	28	0	1247–2090 *1398*	26	0	1230–2113 *1737*	37	0	887–1370 *1099*	55	0	8.38–562 *215*
Mn	0.70	28	0	37.5–230 *134*	26	0	18.9–195 *107*	37	0	33.2–214 *110*	55	0	54.7–153.8 *82.4*
Co	0.40	28	0	18.3–37.1 *25.7*	26	0	18.4–33.5 *25.5*	37	0	20.6–43.7 *27.9*	55	0	9.18–129 *21.9*
Ni	0.50	28	0	53.5–178 *96.2*	26	0	58.4–176 *99*	37	0	26.2–145 *61.0*	55	0	18.7–428 *105*
Cu	0.40	15	13	<0.40–7.47 *3.19*	4	22	<0.40–1.88 *1.17*	15	22	<0.40–228 *41.7*	22	33	<0.40–203 *15.7*
Zn	3.00	19	9	<3.0–31.3 *12.1*	8	18	<3.0–13.9 *9.15*	14	23	<3.0–15.4 *9.34*	30	25	<3.0–19.1 *7.9*
Ga	0.14	28	0	29.1–59.0 *39.2*	26	0	27.9–53.1 *37.0*	37	0	21.1–42.9 *27.9*	55	0	11.2–26.5 *15.3*
Ge	0.80	28	0	2.30–7.50 *5.7*	26	0	4.00–11.9 *6.23*	37	0	4.50–9.50 *6.04*	55	0	2.10–8.20 *6.00*
Sr	0.05	25	3	<0.05–12.0 *5.07*	13	13	<0.05–4.42 *1.07*	28	9	<0.05–7.60 *1.66*	46	9	<0.05–18.4 *5.57*
Y	0.06	17	11	<0.06–3.28 *1.35*	4	22	<0.06–0.34 *0.21*	24	13	<0.06–4.10 *1.10*	38	17	<0.06–6.31 *2.18*
Ba	0.10	25	3	1.22–19.9 *7.41*	9	17	0.15–5.35 *1.71*	27	10	0.35–11.2 *2.28*	43	12	0.30–21.9 *7.65*

All the concentrations are reported in parts per million. The range indicates the minimum and maximum concentration

The average is shown in italics and was calculated considering only values above the DL. Most data below the detection limit of Cr, Sn, Sc, Nb, Mo, and Sb

N number of analyses, *n* number of analyses below detection limit (BDL)

grains include Ti oxides (rutile and ilmenite), clinopyroxene (augite), orthopyroxene (hypersthene–enstatite), amphibole (actinolite–ferroactinolite–pargasite), titanite, and chlorite (clinochlore); the latter is related to amphibole/pyroxene alteration. Type IV magnetite grains display randomly distributed inclusions or forming repetitive sinuous arrangements (Fig. SM2d). Mineral inclusions hosted in type IV magnetite include actinolite, quartz, Na–clinopyroxene (aegirine), and Mg–orthopyroxene (hypersthene–enstatite), which correlate with Mg, Al, and Si magnetite enrichments (Fig. SM3).

Zircon U–Pb dating

Zircons extracted from the diorite intrusion (sample CNN-05) are clear, are light reddish-brown in color, range from 80 to 250 μm in size, and show narrow concentric zoning in CL imaging. They have U and Th concentrations that vary from 1320 to 3846 and 765–4750 ppm, respectively, yielding U/Th ratios of ~ 1, characteristic of igneous zircons (Rubatto 2002). Analyses of 20 zircon grains yielded a weighted average $^{206}Pb/^{238}U$ age of 129.6 ± 1.0 Ma (MSWD = 1.8, $n = 21$;

Fig. 8). No older components were detected. Results for each spot are reported in Table SM3.

Sulfur isotopic compositions

The $\delta^{34}S$ values of Cerro Negro Norte pyrite, mainly from veinlets corresponding to the hydrothermal mineralization event (Fig. 6), were measured in order to elucidate the source of sulfur. The $\delta^{34}S$ values for seven pyrite samples range from -0.5 to $+4.3‰$ (Table SM4) with a mean of $+1.1‰$ and a median of $+0.8‰$. It is noteworthy that no correlation is observed between sample depth and $\delta^{34}S$ values.

Discussion

Timing and sulfur source

The timing of magnetite formation in Cerro Negro Norte is constrained here at ~ 130 Ma by U–Pb zircon dating of the La Brea diorite, which is spatially related to the ore deposit (Fig. 2). This Early Cretaceous age is similar, within uncertainty, to the age obtained for the Carmen (131.0 ± 1.0 Ma; Gelcich et al. 2005) and the El Romeral deposits (129.0 ± 0.9 Ma; Rojas et al. 2018b), where a genetic link between magnetite ore and diorite intrusions has been demonstrated. It is apparent from the limited geochronology for IOA deposits in northern Chile that the period around 130 Ma was very fertile for this type of deposit. In addition, the new age presented here supports the notion that Andean IOA deposits formed under extensional conditions during the first substage of the Andean I period, also known as the Early Pacific stage (135–120 Ma) (Chen et al. 2013).
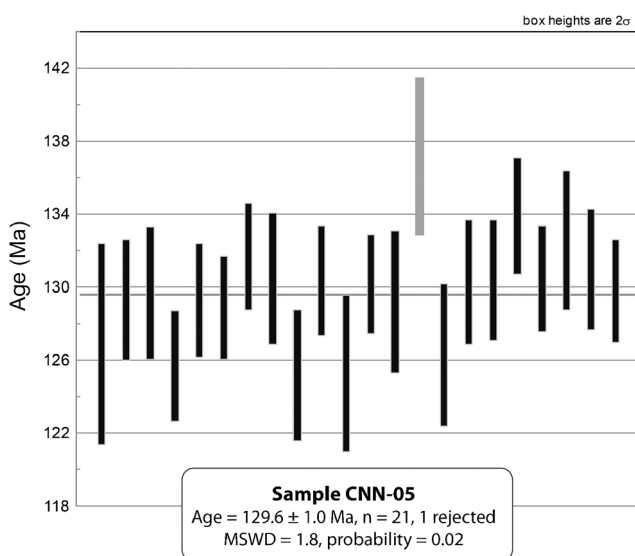

Fig. 8 Weighted average plot for igneous zircons from the diorite intrusion

The sulfur isotopic signature of pyrite from the Cerro Negro Norte deposit varies within a narrow range from -0.5 to $+4.3‰$ (Table SM4), indicating an exclusively magmatic origin without a sedimentary or bacterial contribution. The $\delta^{34}S$ values in this deposit are very similar to those reported for El Romeral and other Andean IOA deposits (Fig. 9), which display a restricted range between -5 and $+5‰$. Andean IOCG deposits (e.g., Candelaria, Diego de Almagro) also display a narrow range of $\delta^{34}S$ values, except Mantoverde where a possible contribution from a non-magmatic source has been proposed (Benavides et al. 2007).

Discrimination diagrams as a fingerprint of deposit types

Several diagrams that use the trace element composition of magnetite have been proposed to discriminate between different deposit types, e.g., porphyry, BIF, Kiruna, IOCG, and Fe–Ti–V deposits (Dupuis and Beaudoin 2011; Nadoll et al. 2014; Meng et al. 2017), or to differentiate between a hydrothermal and a magmatic origin (Dare et al. 2014; Nadoll et al. 2015; Knipping et al. 2015b; Wen et al. 2017). Recent studies from Chilean IOA deposits, e.g., El Laco (Dupuis and Beaudoin 2011; Broughm et al. 2017; Ovalle et al. 2018), Los Colorados (Knipping et al. 2015a, 2015b; Deditius et al. 2018), and El Romeral (Rojas et al. 2018a), show that analyzed magnetite grains plot in all deposit-type fields in the [Ti + V] versus [Al + Mn] diagram. In Cerro Negro Norte, inclusion-rich magnetite cores (type I) have a similar [Ti + V] concentration range than type II magnetite, e.g., 0.13–0.40 wt% and 0.13–0.30 wt%, respectively. On the other hand, the [Al + Mn] concentration is slightly higher in type I magnetite (0.017–0.32 wt%) in comparison with that in type II (0.023–0.21 wt%). The latter shows a more widespread compositional distribution with occasional spots with a higher [Ti + V] and [Al + Mn] content than type I magnetite (Fig. 10). Inclusion-free magnetite grains (type III) have variable concentrations of Al, Mn, Ti, and V, with a high [Al + Mn] (up to 0.29 wt%) and Ti content (up to 0.9 wt%) and moderately high V concentrations (average 1.1 wt%; Table 1). Most analyses from type III magnetite plot in the IOCG and Kiruna fields, whereas type IV magnetite plots in or near the BIF field, displaying the lowest trace element content (Fig. 10). In summary, most of the analyses of Cerro Negro Norte magnetite grains plot between the IOCG, Porphyry, and Kiruna fields, and some plot even below the Kiruna field. Based on the work by Nadoll et al. (2014), Knipping et al. (2015a) showed that the chemical composition of the different magnetite types identified in Los Colorados reflects a cooling trend from high-temperature magmatic (> 500 °C; the Fe–Ti, V field) to high-temperature hydrothermal conditions (300–500 °C; the porphyry and Kiruna fields). A
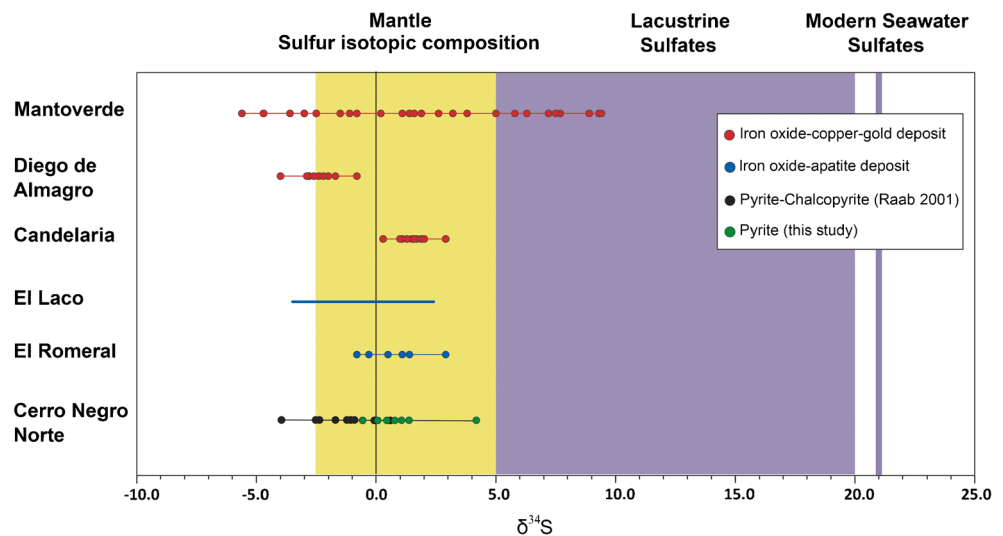
similar cooling trend was also observed for magnetite grains from El Laco (Ovalle et al. 2018).

Although no igneous magnetite has been identified in Cerro Negro Norte, a slight cooling trend is observed for magnetite types I and II (Fig. 10), reflecting a formation from a cooling hydrothermal fluid at temperatures between 300 and 500 °C. On the other hand, type IV magnetite vein mineralization represents a lower temperature mineralization event at 200–300 °C. Thus, our data support the notion that the magnetite composition plotted in the [Al + Mn] versus [Ti + V] diagram reflects the formation temperature, as previously suggested by Nadoll et al. (2014). It follows that the magnetite ore in each Chilean IOA deposit (e.g., Los Colorados, El Romeral, El Laco, and Cerro Negro Norte) is the result of different events and that the trace elements incorporated into

or remobilized from the magnetite grains reflect a strong temperature control; however, other factors such as the composition of the hydrothermal fluids, oxygen and sulfur fugacity, co-precipitation of competing mineral phases, and fluid–rock interactions can also play a significant role in the incorporation of these and other trace elements into magnetite (Nadoll et al. 2014). Based on previous studies and our own observations, elements such as Ti, V, Mn, and Ga are incorporated into magnetite at high temperatures. High concentrations of Na, Mg, Si, K, and Ca in magnetite might be related to silicate inclusions, such as pargasite and actinolite, whereas sulfide nano- to micron-scale inclusions might be responsible for high concentrations of Cu, Co, Ni, and possibly Zn in hydrothermal magnetite. Incorporation of Cr, Sc, Y, Nb, Mo, Sn, and Sb into magnetite is possibly related to the availability of these elements in the source or remobilized from the host rocks.

Magmatic versus hydrothermal magnetite

Several diagrams have been proposed to discriminate between igneous and hydrothermal magnetite, among them Sn versus Ga (Nadoll et al. 2014), Ti versus Ni/Cr (Dare et al. 2014), and V versus Cr (Knipping et al. 2015b). However, Cr is below detection limits in the Cerro Negro Norte magnetite and Sn is less than 2 ppm. Hence, these plots were not used to characterize the origin of magnetite in Cerro Negro Norte.

Another diagram used to discriminate igneous from hydrothermal magnetite in porphyry system was proposed by Nadoll et al. (2015) by comparing the V and Ti concentrations (Fig. 11), owing to the observation that igneous magnetite is ubiquitously enriched in these lithophile elements when compared to hydrothermal magnetite. The Cerro Negro Norte magnetite contains 8.4–2113 ppm V and < 4.0–1990 ppm Ti (Fig. 11; Table 1 and SM2), both consistent with the global range of igneous and hydrothermal magnetite (15–6600 ppm V, < 15–3560 ppm Ti; Nadoll et al. 2015). In general, types I,
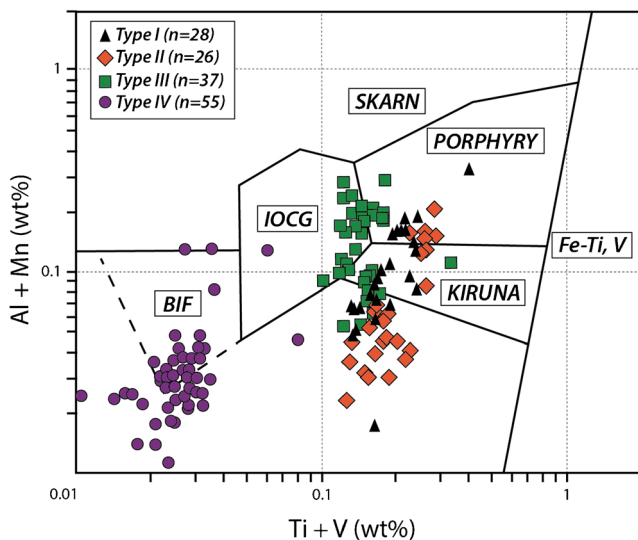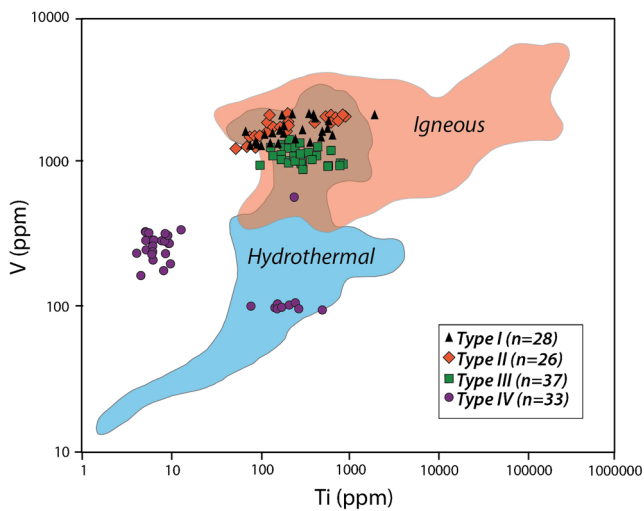

Fig. 10 Chemical discrimination diagram for magnetite after Dupuis and Beaudoin (2011) and modified by Nadoll et al. (2014). Types I and II plot in the Porphyry and Kiruna fields, whereas type III in the IOCG, Kiruna, and Porphyry fields. Magnetite-vein mineralization (type IV) shows the lowest trace element content and plot mostly in the BIF field

Fig. 11 Ti versus V concentration in magnetite. Blue field represents hydrothermal magnetite, whereas the red area is defined by igneous magnetite. The data for Cerro Negro Norte plot mostly in the overlapping area. Type IV magnetite plots in or close to the hydrothermal field. Fields based on data from Nadoll (2011)

II, and III magnetite grains plot in the overlapping area between the magmatic and hydrothermal fields, whereas type IV plots mostly in the hydrothermal area, with a large cluster of

data points showing a V content consistent with hydrothermal magnetite, but with lower Ti concentrations (Fig. 11).

Recently, Wen et al. (2017) proposed a new discrimination diagram based on the Fe content and the V/Ti ratio of magnetite (Fig. 12). This diagram is based on the observation that generally the V/Ti ratio is < 1 and > 1, respectively, in igneous and hydrothermal magnetite, whereas the Fe content tends to decrease in igneous magnetite (< 66 wt% Fe) relative to hydrothermal magnetite because of differential incorporation of trace elements into the magnetite structure. By plotting our results in this diagram with data from other Andean Kiruna-type deposits, such as El Laco (Broughm et al. 2017), Los Colorados (Knipping et al. 2015b), and El Romeral (Rojas et al. 2018a), and analyses of igneous, high-temperature, and low-temperature hydrothermal magnetite (Nadoll 2011; Nadoll et al. 2014, 2015), it is clear that all IOA data points plot within the hydrothermal field and that no re-equilibration trend is observed, with the possible exception of Los Colorados (Fig. 12). In particular, Cerro Negro Norte magnetite grains have a relatively constant Fe content (70–72 wt% Fe) and a variable V/Ti ratio with type IV magnetite having the largest range of V/Ti values. The Ti content among Cerro Negro Norte magnetite grains is variable and ranges from a few tens up to hundreds of parts per million in all types, except for type IV,

Fig. 12 Discrimination diagram proposed by Wen et al. (2017). Data from Cerro Negro Norte and other Andean IOA deposits (El Romeral, Los Colorados, and El Laco) plot in the hydrothermal area
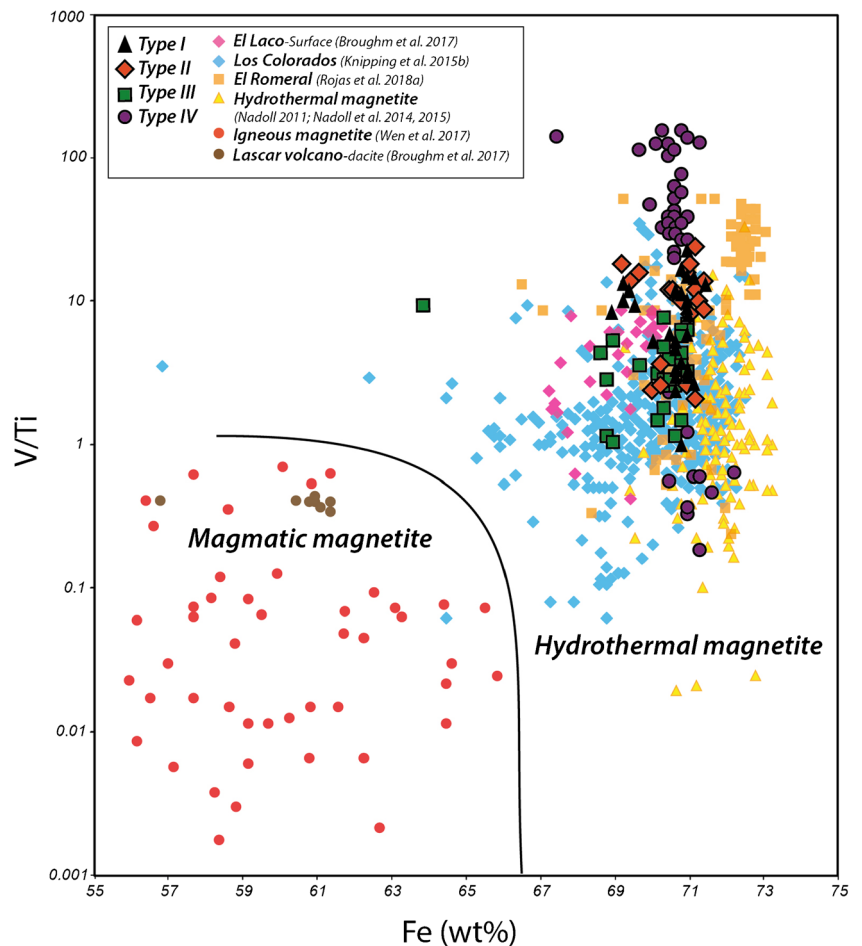
where it can be less than 4 ppm. On the other hand, V is high in type I (mean = 1398 ppm) and II (mean = 1737 ppm) magnetites, slightly lower in type III (mean = 1099 ppm), and significantly lower in type IV magnetite (mean = 215 ppm; Table 1 and Figs. 11, 13). Vanadium is highly compatible and is usually present in high concentrations and homogeneously distributed in IOA magnetite grains (Knipping et al. 2015a, 2015b; Rojas et al. 2018a). The slightly higher average V value found in type II magnetite is probably related to dissolution and reprecipitation processes of type I magnetite.

In addition, some authors have hypothesized that the concentration of Sn and Ga can be used to discriminate different types of hydrothermal magnetite (Kamvong et al. 2007) and igneous magnetite (Nadoll et al. 2014). Average Sn concentration in magnetite from Cerro Negro Norte is ≤ 1 ppm (Table 1), a lower average than those reported for hydrothermal magnetite (Nadoll et al. 2014). On the other hand, a high Ga content (> 60 ppm) appears to be an indicator of high-temperature magnetite crystallization (Nadoll et al. 2014; Knipping et al. 2015b), and thus, a good proxy to trace the evolution of Cerro Negro Norte. In Cerro Negro Norte, the Ga concentration in magnetite ranges from 11.2 to 59 ppm (Table 1). Figure 13 shows a V versus Ga plot for the Cerro Negro Norte, El Laco, and Kiruna IOA deposits, and magnetite from volcanic rocks in which a general trend from high-temperature (magmatic) to low-temperature hydrothermal magnetite is recognized. Here, the Cerro Negro Norte magnetite grains reflect a transition from high-temperature hydrothermal (types I and II) to medium-temperature hydrothermal (type III) and low-temperature hydrothermal conditions (type IV). Thus, the magnetite data for the Cerro Negro Norte deposit reflect different conditions and formation processes, leading to significant textural features

which can be intimately related to chemical variations at both the macro- and micro-scale. Data from the Kiruna deposits in Sweden and from El Laco in northern Chile (Broughmt et al. 2017) are also plotted in Fig. 13. Both El Laco and Kiruna magnetite grains have low Ga (< 20 ppm) and a low to moderate V content, which is more consistent with a hydrothermal origin, as has been suggested for El Laco based on analyses of surface samples by Dare et al. (2015). The low trace element content in Kiruna magnetite ore samples could also reflect a hydrothermal origin or an overprint by metasomatic processes as suggested by Broughm et al. (2017).

Magnetite formation conditions

The data presented in this study reflect the evolution of the Cerro Negro Norte deposit. The deposit is characterized by several formation processes under different conditions that are expressed in significant textural and chemical variations. Based on these chemical and textural features, four events of magnetite mineralization are recognized (Fig. 14): an early event with the formation of inclusion-rich magnetite (type I) followed by precipitation of inclusion-free magnetite (type II), generally observed as rims, growing over type I magnetite. The chemical differences between both types are mainly in the Al, Ti, and Mn concentrations, which decrease in rims (type II), while V and Ga tend to be relatively constant in both types (Table 1). This could be explained by precipitation of high-temperature hydrothermal magnetite over type I magnetite as seen in Los Colorados and El Romeral (Knipping et al. 2015a, b; Rojas et al. 2018a).

Vanadium incorporation into magnetite is mostly favored at low oxygen fugacity and high-temperature conditions (Toplis and Corgne 2002; Nadoll et al. 2014). In addition, both Ti and

Fig. 13 V versus Ga content in magnetite. Type I and II magnetite grains formed under high-temperature hydrothermal conditions. Type III magnetite is associated with moderate temperature hydrothermal fluids, whereas type IV precipitated from low-temperature, high fO_2 hydrothermal fluids. Data for Kiruna magnetite ore, El Laco, and Láscar samples from Broughm et al. (2017)
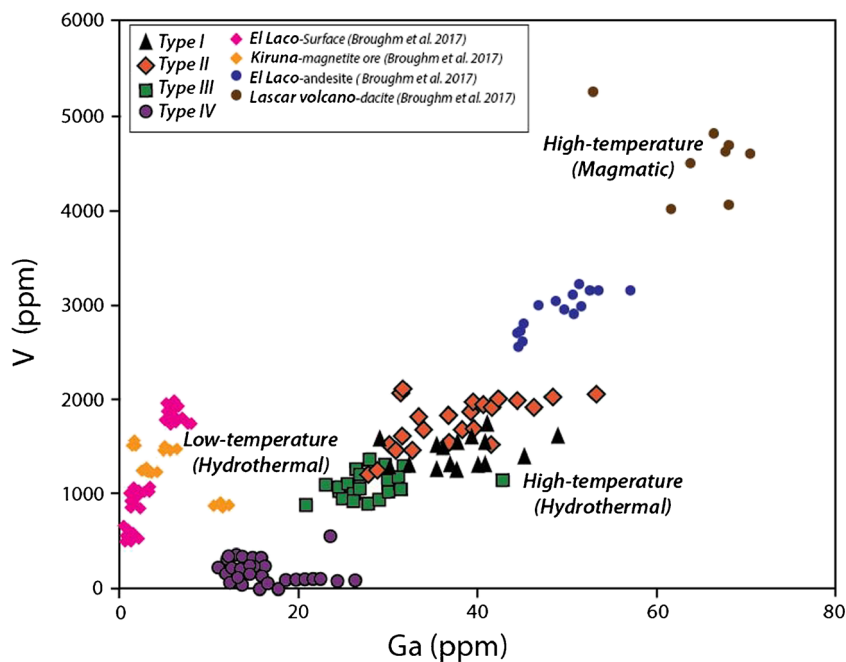
Fig. 14 Schematic model for the formation of magnetite types in Cerro Negro Norte. **a** Crystallization of type I inclusion-rich magnetite from a high-temperature (~ 500 °C) magmatic-hydrothermal fluid. Bubble nucleation allows for ascent and accumulation of magnetite grains. **b** Precipitation of type II inclusion-free magnetite over type I magnetite. **c** Formation of type III magnetite from the cooling hydrothermal fluid. **d** Late magnetite veinlets (type IV magnetite) crosscut all previous magnetite types. This late hydrothermal event is followed by the precipitation of disseminated sulfides and formation of sulfide veinlets
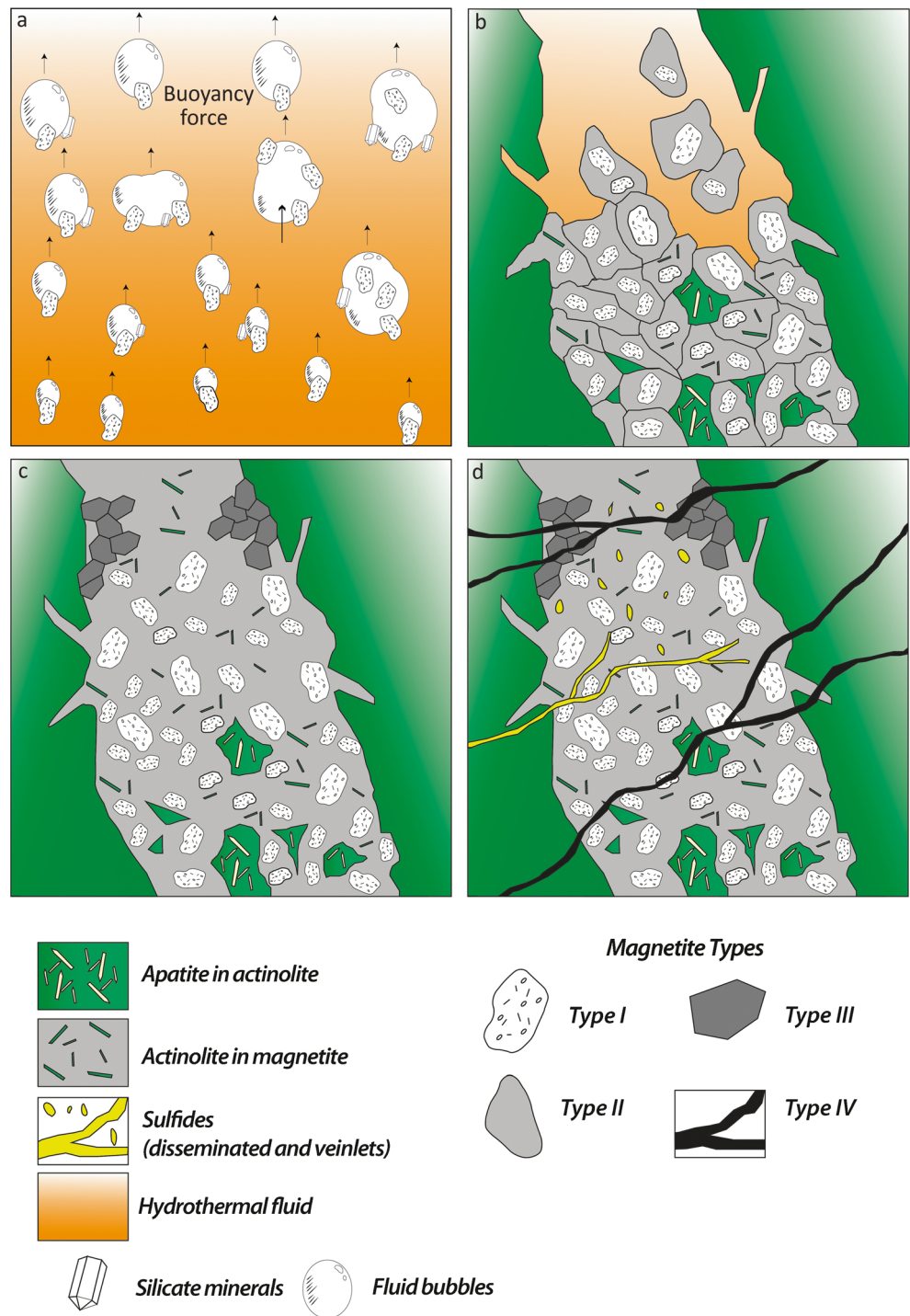
Al are also incorporated into magnetite at higher temperatures and considered immobile at submagmatic temperatures (Van Baalen 1993; Nadoll et al. 2014). It appears then that magnetite grains of types I and II were precipitated at similar high-temperature hydrothermal conditions (~ 500 °C) and at low oxygen fugacity conditions, whereas type III precipitated at an intermediate temperature (~ 300–400 °C). Precipitation of these three different types of magnetite (types I, II, and III) could be related to changes in the composition of the hydrothermal fluid as it cools. On the other hand, the formation of type IV magnetite veinlets is associated with a later metasomatic event characterized by a low temperature (i.e., ~ 200–300 °C) and more oxidized hydrothermal fluid. The relatively high Ti concentration in some analysis of type IV magnetite (up to 509 ppm) is possibly related to dissolution and reprecipitation of type I and type II magnetite, as reported by Ovalle et al. (2018) at El Laco, or most likely to the presence Ti-bearing nanoinclusions such as titanite or rutile.

Mineral inclusions present in type I magnetite grains can provide further insights about formation temperature of primary magnetite if we assume that those inclusions crystallized simultaneously with type I magnetite. As a result of differing nucleation and growth rates, these mineral inclusions would be randomly incorporated within the magnetite host crystals. The presence of abundant high-temperature inclusions in magnetite grain cores has also been described for the Los Colorados (Knipping et al. 2015a, 2015b) and El Romeral (Rojas et al. 2018a), where the cited authors have interpreted these inclusion-rich magnetite cores as a common feature of primary magmatic magnetite.

Several inclusions were identified in type I magnetite from Cerro Negro Norte, such as rutile, ilmenite, pyroxene, actinolite, pargasite, titanite, and clinochlore. At 200 MPa, pargasite stability is estimated between ~ 800 and ~ 1020 °C (Jenkins 1983), whereas clinochlore breaks down at ~ 780 °C (Staudigel and Schreyer 1977). These temperatures are higher than those estimated based on the magnetite chemistry, and hence, it is likely that at least some of these inclusions were formed at magmatic temperatures (~ 800 °C) and trapped within magnetite type I at temperatures close to 500 °C during cooling of the magmatic-hydrothermal system.

Cerro Negro Norte: an IOCG link?

The Compañía Minera del Pacífico (CMP), through studies in the 1980s, recognized the economic potential for the copper and gold reserves at Cerro Negro Norte, estimating total reserves of 550,000 tons at 1.45 g/ton Au and 0.24% Cu. In general, the areas of interest are along late or reactivated fault zones with NNE orientation and contacts between the andesite host rock and the diorite intrusion (Vivallo et al. 1995b).

Three of these Cu–Au-rich zones are located west of the Abanderada area, where abundant quartz + carbonates ± Cu sulfide veinlets are present (Raab 2001; Vivallo et al. 1995b). A fourth zone of interest, towards the north of the same area, is related to andesitic rocks altered to chlorite + calcite + quartz + tourmaline. In the Augusta area (Fig. 3), it is also possible to find Cu–Au mineralization, which is associated mainly with quartz + tourmaline + sericite breccias.

Vivallo et al. (1995b) concluded that higher gold grades (up to 1 ppm) are associated with pyrite mineralization, whereas Au in magnetite is usually less than 100 ppb. These authors suggested a late hydrothermal remobilization of Au from the iron ore of magmatic origin, with the consequent redistribution of Au associated with increased sulfur fugacity in the system. On the other hand, Raab (2001) suggested that the Cu–Au mineralization is predominantly associated with late pyrite ± chalcopyrite veinlets and the tourmaline–quartz alteration. In addition, the abundance of Cu sulfides (mainly chalcopyrite) increases from type III to type IV magnetite-related events, reaching up to a 1:1 pyrite-chalcopyrite ratio in some

samples, which could reflect an increase in the Cu content of the hydrothermal fluids.

Based on our observations, the increasing sulfide content from stage I to stage II is consistent with the IOA flotation model (Knipping et al. 2015a, b; Reich et al. 2016) where the magmatic-hydrothermal fluid can transport and later precipitate magnetite and other metals (i.e., Cu, Au). The sulfides and Au related to the quartz–tourmaline alteration (stage III; Fig. 6) are possibly associated with a later hydrothermal event and not to the main IOA formation.

Conclusions

The Cerro Negro Norte deposit is hosted in Cretaceous volcanic rocks from the Bandurrias Formation and is spatially and genetically related to La Brea diorite intrusion. Uranium–Pb zircon dating of this intrusion yielded a 129.6 ± 1.0 Ma age, which is consistent with other IOAs in the Chilean Iron Belt (e.g., El Romeral, Carmen). The deposit was formed by an early magmatic-hydrothermal episode with magnetite and actinolite followed by the main hydrothermal event, which includes precipitation of hydrothermal magnetite and sulfides. The $\delta^{34}S$ values obtained for pyrite from the Cerro Negro Norte deposit vary between -0.5 and $+4.3\%$, indicating an exclusively magmatic origin for the sulfur in this deposit. This finding is consistent with the sulfur isotopic signature for El Romeral and other Andean IOA and IOCG deposits.

Mineralogical observations combined with microanalytical techniques, i.e., LA-ICP-MS analysis, EPMA, and SEM data, reveal four main magnetite types in Cerro Negro Norte: (i) early magnetite mineralization (type I) represented by high-temperature (~ 500 °C), hydrothermal magnetite cores (type I) with mainly amphiboles, pyroxene, and some oxide inclusions; (ii) inclusion-free hydrothermal magnetite (type II), usually surrounding type I magnetite and formed at similar high temperatures; (iii) type III magnetite is generally inclusion free but may have few inclusions, oscillatory, and chemical zoning formed at intermediate temperatures (~ 300–400 °C); and (iv) late hydrothermal magnetite veinlets (type IV) with sinuous oscillatory inclusion arrangements and precipitated at low temperatures (~ 200–250 °C). The magnetite grains show a variable concentration of trace elements that reflect their formation temperature, the element availability in the cooling hydrothermal fluid, and the redox conditions. Based on the chemical characteristics of the magnetite types, a new discrimination diagram based on the V and Ga concentrations is proposed to identify magmatic or hydrothermal events.

The data presented here for the Cerro Negro Norte deposit are consistent with the flotation model as proposed for Los Colorados (Knipping et al. 2015a, 2015b) and supported by further evidence from the El Romeral iron deposit (Rojas et al. 2018a, 2018b); however, no high-temperature (>

500 °C) magmatic magnetite was identified in our study. This suggests that the iron ore body could extend to deeper levels where a magmatic component remains to be found. The use of discrimination diagrams (Dupuis and Beaudoin 2011; Dare et al. 2014; Knipping et al. 2015a; Wen et al. 2017) should be coupled with detailed petrographic and textural studies in order to characterize superimposed metasomatic events that can modify the trace element signature of magnetite as has been reported for Kiruna, Sweden, by Broughm et al. (2017). Furthermore, the presence, formation, and composition of microinclusions and nanoparticles play a critical role in the interpretation of chemical data in magnetite (Deditius et al. 2018). In our case study, it is the V versus Ga plot that best represents the four magnetite-bearing mineralization events recognized in the Cerro Negro Norte deposit allowing for a better discrimination between magmatic and hydrothermal magnetite.

References

Aguirre L (1985) The southern Andes. In: Nairn AEM, Stehli FG, Uyeda S (eds) The ocean basins and margins. Springer, Boston, MA, pp 265–376

Arévalo C (1995) Mapa Geológico Hoja Copiapó, Región de Atacama, escala 100,000. Servicio Nacional de Geología y Minería

Arévalo C (2005) Carta Copiapó, Región de Atacama. 54 p., 1 map escala 1:100,000. Servicio Nacional de Geología y Minería

Barra F, Reich M, Selby D, Rojas P, Simon A, Salazar E, Palma G (2017) Unraveling the origin of the Andean IOCG clan: a Re-Os isotope approach. Ore Geol Rev 81:62–78

Barton MD (2014) Iron oxide (-Cu-Au-REE-P-Ag-U-Co) systems. In: Holland H and Turkian K (eds) Treatise in Geochemistry 2nd Edition 13:515–541

Benavides J, Kyser TK, Clark AH, Oates CJ, Zamora R, Tarnovschi R, Castillo B (2007) The Mantoverde iron oxide-copper-gold district, III Región, Chile: the role of regionally derived, nonmagmatic fluids in chalcopyrite mineralization. Econ Geol 102:415–440

Bilenker LD, Simon AC, Reich M, Lundstrom CC, Gajos N, Bindeman I, Barra F, Munizaga R (2016) Fe-O stable isotope pairs elucidate a high-temperature origin of Chilean iron oxide-apatite deposits. Geochim Cosmochim Acta 177:94–104

Black LP, Kamo SL, Allen CM, Davis DW, Aleinikoff JN, Valley JW, Mundil R, Campbell IH, Korsch RJ, Williams IS, Foudoulis C (2004) Improved Pb-206/U-218 microprobe geochronology by the monitoring of a trace-element-related matrix effect; SHRIMP, IDTIMS, ELA-ICP-MS and oxygen isotope documentation for a series of zircon standards. Chem Geol 205:115–140

Broughm SG, Hanchar JM, Tornos F, Westhues A, Attersley S (2017) Mineral chemistry of magnetite from magnetite-apatite mineralization and their host rocks: examples from Kiruna, Sweden, and El Laco, Chile. Mineral Deposita 52:1223–1244

CAP Minería Annual Report (2016) http://www.cap.cl/cap/site/artic/20170331/asocfile/20170331175859/memoria_cap_2016.pdf. Accessed 27 June 2018

Chen H, Cooke DR, Baker MJ (2013) Mesozoic iron oxide copper-gold mineralization in the Central Andes and the Gondwana supercontinent breakup. Econ Geol 108:37–44

Coleman ML, Moore MP (1978) Direct reduction of sulfates to sulfur dioxide for isotopic analysis. Anal Chem 50:1594–1595

Dare SAS, Barnes S-J, Beaudoin G, Méric J, Boutroy E, Potvin-Doucet C (2014) Trace elements in magnetite as petrogenetic indicators. Mineral Deposita 49:785–796

Dare SAS, Barnes S-J, Beaudoin G (2015) Did the massive magnetite "lava flows" of El Laco (Chile) form by magmatic or hydrothermal processes? New constraints from magnetite composition by LA-ICP-MS. Mineral Deposita 50:607–617

Deditius AP, Reich M, Simon AC, Suvorova A, Knipping J, Roberts MP, Rubanov S, Dodd A, Sauders M (2018) Nanogeochemistry of hydrothermal magnetite. Contrib Mineral Petrol 173:46. https://doi.org/10.1007/s00410-018-1474-1

Dupuis C, Beaudoin G (2011) Discriminant diagrams for iron oxide trace element fingerprinting of mineral deposit types. Mineral Deposita 46:319–335

Espinoza S (1990) The Atacama-Coquimbo ferriferous belt, northern Chile. In: Fontboté L, Amstutz GC, Cardozo M, Cedillo E, Frutos J (eds) Stratabound ore deposits in the Andes. Springer-Verlag, Berlin, pp 353–364

Gelcich S, Davis DW, Spooner ETC (2005) Testing the apatite-magnetite geochronometer: U-Pb and $^{40}Ar/^{39}Ar$ geochronology of plutonic rocks, massive magnetite-apatite tabular bodies, and IOCG mineralization in Northern Chile. Geochim Cosmochim Acta 69:3367–3384

Grocott J, Taylor GK (2002) Magmatic arc fault systems, deformation partitioning and emplacement of granitic complexes in the Coastal Cordillera, north Chilean Andes (25°30'S to 27°00'S). J Geol Soc 159:425–443

Jenkins DM (1983) Stability and composition relations of calcic amphiboles in ultramafic rocks. Contrib Mineral Petrol 83:375–384

Kamvong T, Zaw K, Siegele R (2007) PIXE/PIGE microanalysis of trace elements in hydrothermal magnetite and exploration significance: a pilot study. 15th Australian Conference on Nuclear and Complementary Techniques of Analysis and 9th Vacuum Society of Australia Congress. University of Melbourne, Melbourne, Australia

Knipping JL, Bilenker LD, Simon AC, Reich M, Barra F, Deditius AP, Lundstrom C, Bindeman I, Munizaga R (2015a) Giant Kiruna-type deposits form by efficient flotation of magmatic magnetite suspensions. Geology 43:591–594

Knipping JL, Bilenker LD, Simon AC, Reich M, Barra F, Deditius AP, Wälle M, Heinrich CA, Holtz F, Munizaga R (2015b) Trace elements in magnetite from massive iron oxide-apatite deposits indicate a combined formation by igneous and magmatic-hydrothermal processes. Geochim Cosmochim Acta 171:15–38

Knipping JL, Fiege A, Simon AC, Oeser M, Reich M, Bilenker L (2019) In-situ iron isotope analyses reveal igneous and magmatic-hydrothermal growth of magnetite at the Los Colorados Kiruna-type iron oxide−apatite deposit. Am Mineral, Chile. https://doi.org/10.2138/am-2019-6623

Lara L, Godoy E (1998) Hoja Quebrada Salitrosa, Región de Atacama. Servicio Nacional de Geología y Minería (SERNAGEOMIN), Mapas Geológicos, 1:100,000 scale, No. 4

Loberg BEH, Horndahl A-K (1983) Ferride geochemistry of Swedish Precambrian iron ores. Mineral Deposita 18:487–504

Longerich HP, Jackson SE, Günther D (1996) Laser ablation inductively coupled plasma mass spectrometric transient signal data acquisition and analyte concentration calculation. J Anal At Spectrom 11:899–904

Loyola N (2016) Origen de la mineralización y alteración hidrotermal del depósito tipo IOCG Diego de Almagro, III Región de Atacama, Chile. Honours thesis, Universidad de Chile, Santiago, Chile, 130 pp.

Ludwig K (2010) Isoplot/Ex version 4.1, a geochronological toolkit for Microsoft Excel: Berkeley Geochronology Center, Special Publication No. 4

Marschik R, Fontboté L (2001) The Candelaria-Punta del Cobre iron oxide Cu-Au(-Zn-Ag) deposits, Chile. Econ Geol 96:1799–1826

McInnes BIA, Keays RR, Lambert DD, Hellstrom J, Allwood JS (2008) Re–Os geochronology and isotope systematics of the Tanami, Tennant Creek and Olympic Dam Cu–Au deposits. Aust J Earth Sci 55:967–981

Ménard J (1995) Relationship between altered pyroxene diorite and the magnetite mineralization in the Chilean Iron Belt, with emphasis on the El Algarrobo iron deposits (Atacama region, Chile). Mineral Deposita 30:268–274

Meng Y, Hu R, Huang X, Gao J (2017) Germanium in magnetite: a preliminary review. Acta Geol Sin 91:711–726

Mpodozis C, Ramos VA (1990) The Andes of Chile and Argentina. In: Ericksen E, Cañas Pinochet T, Reinemund A (eds) Geology of the Andes and its Relation to Hydrocarbon and Mineral Resources. Circum-Pacific Council for Energy and Mineral Resources, Earth Science Series 11:59–90

Nadoll P (2011) Geochemistry of magnetite from hydrothermal ore deposits and host rocks –case studies from the Proterozoic Belt Supergroup, Cu-Mo-porphyry + skarn and Climax-Mo deposits in the western United States. PhD thesis, The University of Auckland, 313 p

Nadoll P, Koenig AE (2011) LA-ICP-MS of magnetite: methods and reference materials. J Anal At Spectrom 26:1872–1877

Nadoll P, Angerer T, Mauk JL, French D, Walshe J (2014) The chemistry of hydrothermal magnetite: a review. Ore Geol Rev 61:1–32

Nadoll P, Mauk JL, Richard AL, Koenig AE (2015) Geochemistry of magnetite from porphyry cu and skarn deposits in the southwestern United States. Mineral Deposita 50:493–515

Nyström JO, Henríquez F (1994) Magmatic features of iron ores of the Kiruna type in Chile and Sweden: ore textures and magnetite geochemistry. Econ Geol 89:820–839

Ovalle JT, La Cruz NL, Reich M, Barra F, Simon AC, Konecke B, Rodriguez-Mustafa MA, Childress T, Deditius A, Morata D (2018) Formation of massive iron deposits linked to explosive volcanic eruptions. Sci Rep UK 8:14855

Paton C, Hellstrom J, Paul B, Woodhead J, Hergt J (2011) Iolite: freeware for the visualisation and processing of mass spectrometric data. J Anal At Spectrom 26:2508–2518

Raab A (2001) Geology of the Cerro Negro Norte Fe-oxide (Cu-Au) District, Coastal Cordillera, northern Chile. MSc thesis, Oregon State University, 273

Reich M, Simon AC, Deditius A, Barra F, Chryssoulis S, Lagas G, Tardani D, Knipping J, Bilenker L, Sánchez-Alfaro P, Roberts MP, Munizaga R (2016) Trace element signature of pyrite from the Los Colorados Iron oxide-apatite (IOA) deposit, Chile: a missing link between Andean IOA and iron oxide copper-gold systems. Econ Geol 111:743–761

Rieger AA, Marschik R, Díaz M, Hölzl S, Charadia M, Akker B, Spangenberg JE (2010) The hypogene iron oxide copper-gold mineralization in the Mantoverde district, northern Chile. Econ Geol 105:1271–1299

Rojas P, Barra F, Deditius A, Reich M, Simon A, Roberts M, Rojo M (2018a) New contributions to the understanding of Kiruna-type iron oxide-apatite deposits revealed by magnetite ore and gangue mineral geochemistry at the El Romeral deposit, Chile. Ore Geol Rev 93:413–435

Rojas P, Barra F, Reich M, Deditius A, Simon A, Uribe F, Romero R, Rojo M (2018b) A genetic link between magnetite mineralization and diorite intrusion at the El Romeral iron oxide-apatite deposit, northern Chile. Mineral Deposita 53:947–966. https://doi.org/10.1007/s00126-017-0777-x

Rubatto D (2002) Zircon trace element geochemistry; partitioning with garnet and the link between U-Pb ages and metamorphism. Chem Geol 184:123–138

Ruiz FC, Corvalán J, Klohn C, Klohn E, Levi B (1965) Geología y yacimientos metalíferos de Chile. Instituto de Investigaciones Geológicas, Santiago, p 305

Segerstrom K (1968) Geología de las hojas Copiapó y Ojos del Salado, Provincia de Atacama. Instituto de Investigaciones Geológicas, Boletín No 24:58

Sillitoe RH (2003) Iron oxide-copper-gold deposits: an Andean view. Mineral Deposita 38:787–812

Sillitoe RH, Burrows DR (2002) New field evidence bearing on the origin of the El Laco magnetite deposit, northern Chile. Econ Geol 97:1101–1109

Simon AC, Knipping J, Reich M, Barra F, Deditius A, Bilenker L, Childress TA (2018) Kiruna-type iron oxide-apatite (IOA) and iron oxide copper-gold (IOCG) deposits form by a combination of igneous and magmatic-hydrothermal processes: evidence from the Chilean Iron Belt. Soc Econ Geol (SEG): Special Publications 21:89–114

Sláma J, Košler J, Condon D, Crowley J, Gerdes A, Hanchar J, Horstwood M, Morris G, Nasdala L, Norberg N, Schaltegger U, Schoene B, Tubrett M, Whitehouse M (2008) Plešovice zircon — a new natural reference material for U–Pb and Hf isotopic microanalysis. Chem Geol 249:1–35

Staudigel H, Schreyer W (1977) Upper thermal stability of clinochlore at PH$_2$O = 10-35 kb. Contrib Miner Petrol 61:187–198

Toplis MJ, Corgne A (2002) An experimental study of element partitioning between magnetite, clinopyroxene and iron-bearing silicate liquids with particular emphasis on vanadium. Contrib Miner Petrol 144:22–37

Tornos F, Velasco F, Hanchar JM (2016) Iron-rich melts, magmatic magnetite, and superheated hydrothermal systems: The El Laco deposit, Chile. Geology 44(6):427–430

Van Baalen MR (1993) Titanium mobility in metamorphic systems: a review. Chem Geol 110:233–249

Vivallo W, Henríquez F, Espinoza S (1995a) Metasomatismo y alteración hidrotermal en el distrito ferrífero Cerro Negro Norte, Copiapó, Chile. Rev Geol Chile 22:75–88

Vivallo W, Espinoza S, Henríquez F (1995b) Los depósitos de hierro del tipo magnetita-apatita: geoquímica de las rocas volcánicas asociadas y potencialidad de la mena de hierro como fuente de mineralización de oro. Rev Geol Chile 22:159–175

Wen G, Li JW, Hofstra A, Koenig AE, Lowers HA, Adams D (2017) Hydrothermal reequilibration of igneous magnetite in altered granitic plutons and its implications for magnetite classification schemes: insights from the Handan-Xingtai iron district, North China Craton. Geochim Cosmochim Acta 213:255–270

Williams PJ, Barton MD, Johnson DA, Fontboté L, De Haller A, Mark G, Oliver NHS, Marschik R (2005) Iron oxide copper-gold deposits: geology, space-time distribution, and possible modes of origin. In: Hedenquist JW, Thompson JFH, Goldfarb RJ, Richards JP (eds) Economic Geology 100th Anniversary Volume. Society of Economic Geologists, Littleton CO, pp 371–405

Zhimin Z, Yali S (2013) Direct re-Os dating of chalcopyrite from the Lala IOCG deposit in the Kangdian copper belt, China. Econ Geol 108:871–882